

Spatial resolution calculation for the DBES diagnostics on the JT-60SA tokamak

TDK Paper

Asztalos Örs, Master student

Supervisor:

Dr. Pokol Gergő, associate professor

Budapest University of Technology and Economics, Faculty of Natural Sciences,
Department of Nuclear Techniques

BME 2015

TÉRBELI FELBONTÁS SZÁMOLÁS A JT60-SA TOKAMAK DBES DIAGNOSZTIKÁIN
Asztalos Örs

Nukleáris Technikai Intézet

Budapesti Műszaki és Gazdaságtudományi Egyetem

Kivonat

A nyaláb emissziós spektroszkópia (BES) egy aktív plazmadiagnosztikai eszköz, amely a semleges atom és plazma kölcsönhatására épül. Ilyen berendezés építését tervezik az európai-japán együttműködésben épülő JT60-SA szupravezető tokamakra is. A BES rendszer egy nagy energiájú semleges atomnyalábot lő a plazmába, majd optikai megfigyelő rendszerrel követi a nyalábevolúciót az adott közegen belül. A semleges nyaláb plazmával való kölcsönhatása következtében a nyaláb atomjai gerjesztődnek. Ezt követően a legerjesztés és spontán emisszió során kibocsátott karakterisztikus sugárzás alapján rekonstruálható a plazmasűrűség [1].

A RENATE szimulációs program [2] követi az atomnyaláb evolúcióját a plazmán belül. A szimulációs program atomfizika modulja megoldja nyaláb mentén a rátaegyenleteket. A megfigyelt atomi szint emissziója arányos az illető szint elektron populációjával, így meghatározható a nyaláb mentén az emisszióeloszlás.

A RENATE szimulációs program a JT60-SA tokamakon üzemelő fűtőnyaláb semleges atomnyaláb emissziós diagnosztikák modellezésére alkalmaztam (DBES). Fő célom a diagnosztikák térbeli felbontásának meghatározása fluktuációválasz számolása által, amihez a meglévő eljárások mellett [3] új modulok kifejlesztésére is szükség volt. Mivel a JT60-SA tokamak még tervezés alatt áll, és nagy számú atomnyaláb és megfigyelőrendszer pozíció lehetséges, az optimális megfigyelési pozíció meghatározását segítő modul írása vált szükségessé. Egy kiválasztott mérési elrendezésre ezután összevettem a térbeli felbontás számolására alkalmas módszereket.

Contents

1	Introduction	3
1.1	The tokamak	5
1.2	JT-60SA tokamak	6
2	Beam Emission Spectroscopy diagnostics	9
2.1	The RENATE simulation tool	11
2.1.1	Spatial resolution calculation	14
2.2	JT-60SA NBI systems	15
3	Optimal Observation Module	18
3.1	Software development	18
3.1.1	Optimal observation points	19
3.1.2	Doppler shift	21
3.2	Simulations on the JT-60SA NBI systems	23
3.2.1	Simulation data	23
3.2.2	NBI beams #7 and #8	26
3.2.3	NBI beams #9 and #10	33
3.2.4	N-NBI beams	35
3.3	Recommended scenarios	38
4	Benchmarking	40
4.1	Plasma edge scenario	41
4.2	Plasma core scenario	44
4.3	N-NBI scenario	46
5	Conclusions and outlook	49

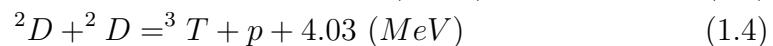
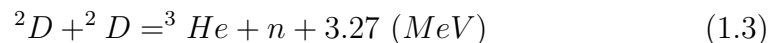
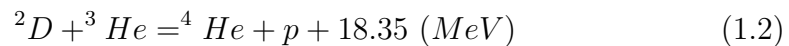
Chapter 1

Introduction

Fusion energy production holds promise to be a viable, long-term process to harness energy with very little or no consequences to the environment. Although plenty of successful research has been conducted into the development and understanding of the physics and technologies behind this promising process, an artificial, stable and reliable fusion based energy source yet remains elusive.

Nuclear fusion is a nuclear reaction during which two atomic nuclei collide at very high velocities resulting in a new, heavier type of atomic nucleus that is accompanied by a release of considerable energy in the case of lighter elements, whereas the process turns out to be endothermic for the heavier elements. Moreover, thermonuclear fusion is the process which aims to achieve nuclear fusion by the use of extremely high temperatures. The major obstacle in this process is overcoming the Coulomb barrier, which requires temperatures in the range of 100 million Kelvin [4]. The light isotopes taking part in the fusion reaction are in a plasma state, which is a high energy, quasi-neutral state, formed out of ions, electrons and a smaller amount of impurities. A more rigorous approach defines plasmas as being quasi neutral, collective and ionized [5].

The most common fusion reactions to occur in a fusion device are as follows [6](deuterium is referred to as: 2D , while tritium is referred to as: 3T):



Reactions (1.1) and (1.2) release considerably more energy than reactions

(1.3) and (1.4). In the case of fusion plasmas, D-T reactions are preferred, because they have the highest reaction rates at considerably lower plasma temperatures. The reaction rates are highest at 85 keV ion temperature [7]. Reaction rates specific to fusion plasmas are given by the rate coefficients and determine the frequency of certain reactions.

$$R = \langle v\sigma \rangle = \int_0^\infty \sigma(v)v f(T, v) dv \quad (1.5)$$

Equation eq.(1.5) gives R , which is the rate coefficient, that describes the reaction probability of a certain event in the plasma, σ is the velocity dependent cross-section of the event in question, $f(T, v)$ is a particle distribution function in velocity space, which is close Maxwellian for fusion plasmas and v is the particle velocity. To arrive at the reaction frequency, the local plasma density has to be taken into consideration as well, by multiplying it with the rate coefficients [8].

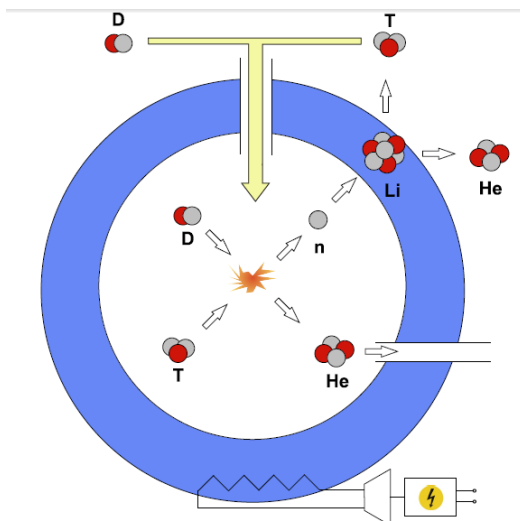
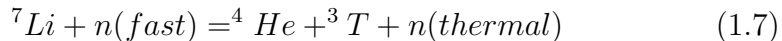


Figure 1.1: *Conceptual design of a fusion power plant with tritium breeder [9].*

The main goal of fusion based energy production is the creation of a steady and reliable energy source. Fuel abundance is a critical issue regarding the continuous operation of any fusion device using deuterium and tritium as a fuel source. Although deuterium is plentiful in nature (D:H ratio in seawater being 1.6×10^{-4}), tritium is a rather scarce, short-lived isotope, having a half-life of $T_{1/2} \approx 12$ years. A steady supply of tritium ensures continuous operation, which becomes viable by building a tritium breeder around the fusion device. Reaction (1.1) shows that some of the energy is released in the

form of He for plasma heating, however the bulk of it is released in the form of neutrons [10].



Reactions (1.6) and (1.7) show the means by which the tritium breeder is harnessing the released neutrons, with the purpose of resupplying the fusion device with tritium, as seen in Figure 1.1, that show a schematic diagram of a tritium breeder built around a fusion device.

1.1 The tokamak

Realization of the thermonuclear fusion process requires extraordinary conditions, especially in regard of overcoming the Coulomb barrier. The realization of such conditions and the necessary plasma confinement, constitutes one of the most defining challenges regarding fusion based energy production. There are two viable plasma confinement possibilities, inertial confinement and magnetic confinement.

The inertial plasma confinement concept relies on the short timed confinement of high density $D - T$ plasmas. This is achieved by the placement of a $D - T$ fuel pellet, coated with an evaporating outer layer, into a high-energy laser field. The heated outer layer explodes outward, producing a reaction force against the remainder of the target, accelerating it inwards, compressing the target. This process is designed to create shock waves that travel inward through the target. A sufficiently powerful set of shock waves can compress and heat the fuel at the center so much that fusion reactions occur. Fusion devices operating under the above mentioned principle can function only in pulsed operation modes [11].

The second concept relies on magnetic fields for confinement. A successful approach relies on superposing magnetic fields. The plasma is confined into torus, a toroidal magnetic field is created by an array of "D" shaped magnetic coils placed around the torus in poloidal planes, creating a toroidal magnetic field. The superposing magnetic field is poloidal, created by a current driven through the plasma in toroidal direction. The current is induced by an increasing current run through a solenoid placed in the center of the device [12, 13].

Figure 1.2 shows a tokamak schematic. The poloidal field coils, creating the toroidal magnetic field are marked with red, while the solenoid driving

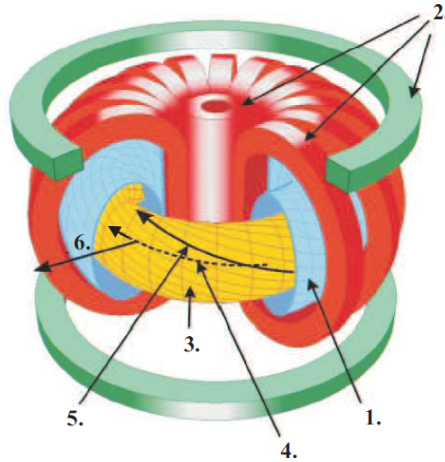


Figure 1.2: Tokamak schematic. 1.-vacuum chamber, 2.-magnetic field coils, 3.-plasma, 4.-plasma current, 5.-magnetic field line, 6.-radial direction [3].

the current through the plasma is located in the center of the device, marked with red as well. Marked with green are vertical field coils responsible for plasma shaping and positioning [12, 13].

From an ideal magneto-hydrodynamic point of view there is the following relation between pressure(p), plasma current(\mathbf{j}) and the magnetic field(\mathbf{B}) characteristic for all fusion devices:

$$\nabla p = \mathbf{j} \times \mathbf{B} \implies \nabla p \perp \mathbf{j} \quad \text{and} \quad \nabla p \perp \mathbf{B} \quad (1.8)$$

Due to the fact that the magnetic field lines and the beam current is perpendicular to the pressure gradient, the field lines form closed surfaces, called flux surfaces. Energy and particle transport is considerably higher along magnetic field lines, which causes intensive plasma properties to have only very small variations on given surfaces [14].

1.2 JT-60SA tokamak

The JT-60SA experiment is one of the three projects to be undertaken in Japan as part of the Broader Approach Agreement, conducted jointly by Europe and Japan. The JT-60SA device is a fully superconducting tokamak capable of confining break-even equivalent deuterium plasmas with equilibria covering high plasma shaping with a low aspect ratio at a high plasma current. The Broader Approach (BA) Activities are the outcome of the privileged partnership established between Europe and Japan at the time of

signature of the ITER Agreement in 2006 [15, 16]. The main missions of the JT-60SA project are as follows:

- Optimize non-inductive current drive for DEMO scenario
- Fully superconducting tokamak operations
- Demonstrate steady state operation at high $\beta(> 4.5)$ for 100 s and more
- Optimize ITER-relevant plasma scenarios and test new operating scenarios
- Test and optimize auxiliary systems which may find an application on ITER
- Advance the understanding of the ITER-relevant physics issues

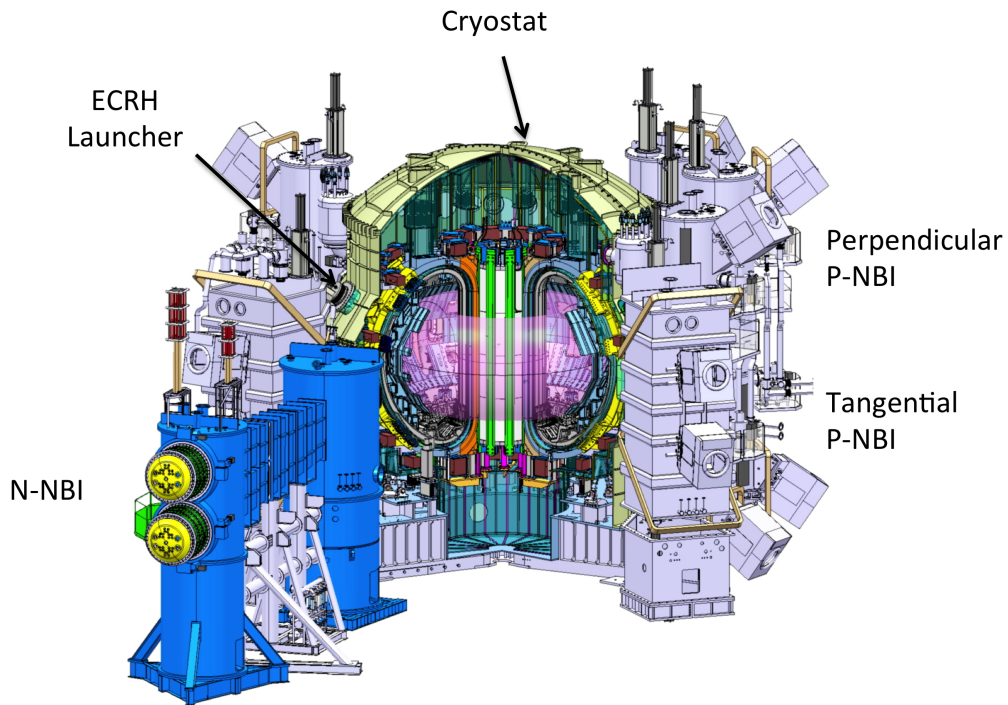


Figure 1.3: Schematic of the JT-60SA tokamak with various heating systems.

Figure 1.3 show a schematic of the JT-60SA tokamak, the vacuum vessel, inside of it the plasma (purple), the cryostat as well as various heating

elements, such as the ERCH heating system as well as NBI heating systems, which will be discussed further on in a plasma diagnostic capacity. The main parameters of JT-60SA [15, 16] as shown in Table.1.1.

Table 1.1: *Tokamak parameters*

Physical parameter	Abbreviation	Value
Toroidal field	$B_t[T]$	2.26
Plasma current	$I_p[MA]$	5.5
Major radius	$R_0[m]$	2.98
Minor radius	$a[m]$	1.18
Aspect ratio	$R/a[-]$	2.50
Elongation	$K[-]$	1.94
Heating and CD power	$[MW] \times [s]$	41×100
Electron cyclotron resonance heating	$ECRH[MW]$	7
Neutral beam injection	$NBI[MW]$	34

Chapter 2

Beam Emission Spectroscopy diagnostics

Magnetically confined plasmas have a temperature range of several million Kelvins, as seen in Chapter. 1, therefore no traditional measuring methods can be applied. All measurement methods developed for the purpose of fusion plasma study are referred to as plasma diagnostics. Plasma diagnostics may be divided into two groups regarding their interaction with the plasma.

Passive plasma diagnostics rely on the observation and the study of particles and photons which are spontaneously emitted or ejected from the plasma without any interference from the outside. These measurements carry the advantage of not causing any perturbation in the plasma.

Active plasma diagnostics rely on the observation of plasma interactions with particles and photons, which are induced by an external source. These measurements carry the advantage of being very localized even though they deliberately cause a perturbation in the plasma.

Beam Emission Spectroscopy (BES) diagnostic systems are active plasma diagnostics which rely on the interaction of plasma with neutral atoms. A high energy beam of neutral atoms is shot into the plasma. Due to collisional events that occur during beam penetration, the electrons get excited onto higher energy levels and then are de-excited emitting characteristic radiation, before ionization. Upon ionization the electrons and ions get caught in the tokamaks magnetic field and are consequently lost from the beam [17]. Employing a specific observation systems, that detects the characteristic light emission for a certain beam type, allows for the monitoring of the electron population on the relevant electron energy levels. The electron population evolution determines the light intensity distribution along the beam. As can be expected, the emission is highest at the plasma edge and diminishes towards the plasma interior. This method is employed to determine especially

plasma density profiles and density fluctuations, due to the fact that the characteristic light emission is determined by the electron population of the corresponding atomic level of the neutral atoms along the beam [18].

Hydrogen and deuterium beams are also used for diagnostic purposes, but only in a secondary capacity. These are high powered beams that primarily serve as heating beams, so called **N**eutral **B**eam **I**njection(NBI) systems. Due to the similar mass of the beam material with the plasma particles, the energy transfer is much more efficient for H and D beams than for any alkali beam, therefore these beams are mainly used for heating purposes and in for refuelling [19]. The beam evolution of the NBI beams is the same as for the alkali beams. Using a well position optical system, optimized for good spatial resolution, the NBI system may be used for diagnostic purposes as well. The beam constitution and high beam velocity allows for much deeper plasma penetration and even core observations. However this system perturbs the plasma at a far greater rate.

Other beam types commonly used in BES diagnostic systems are made of alkali metals, because they possess only one valence electron, thus can be considered hydrogen-type. The obvious advantage in using hydrogen-type atoms lies not only in the beam generation technology, but also the evolution of only one electron has to be monitored. For plasma edge studies, the preferred alkali atom used for the neutral beam is lithium. Sodium beams are used as well, but they provide lower plasma penetration due to the increase in atomic mass, which means smaller beam velocities at certain energies, on the other hand the free valence electron in case of the sodium is bound more loosely to the atom than in the case of the lithium. The LiBES system is especially suited for pedestal and plasma edge observations, while NaBES systems are proven to be more adequate for Scrape Off Layer (SOL) observations, due to their low beam penetration and improved resolution in low density regions of the plasma. BES systems are mainly used for plasma density and density fluctuation measurements [20, 21].

All beam injection systems have the same components. The ion source is regularly a thermal ion source for smaller systems such as lithium or sodium beam, larger systems, such as the NBI heating systems have radio frequency based ion sources. The ions are accelerated to terminal velocity by a single grid or a focusing grid system. The accelerated ions pass through the neutraliser, which for a range of 40 – 80 *keV* provides 70 – 80 % neutralisation. With an increase of beam energy the neutralisation coefficient drops dramatically to barely significant levels. For high energy beams of several 100 *keV* a negative ion source is required, with an electron stripping neutraliser, which holds at 50 – 60 % neutralisation for beam energies up to 1 *MeV*, which is of utmost importance in the case of the 1 *MeV* and 500 *keV* NBI beams to

be installed on ITER and JT-60SA respectively [22].

2.1 The RENATE simulation tool

The RENATE simulation tool is designed to model an injected neutral beam into the plasma, as well as the observation system, calculating the amount of observed light and spatial resolution among other features. RENATE is an acronym for **R**ate **E**quation for **N**eutral **A**lkalibeam **T**Echnique. It is a simulation tool written in IDL programming language. The simulation tool is of modular design [2, 8].

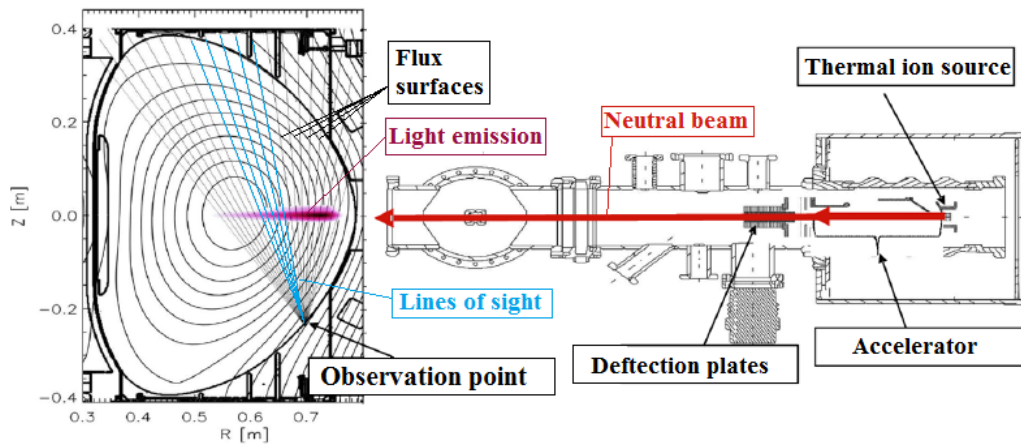


Figure 2.1: The COMPASS LiBES system and the RENATE simulation output for the poloidal cross-section of the tokamak. The plotted poloidal plane contains the beam evolution [3].

The **device module** handles all data regarding the specific device, simulations are performed on. This module handles magnetic geometries, density and temperature profiles as well as impurities. It allocates the appropriate density and temperature values for all flux surfaces. The flux surfaces and device contours in Figure 2.1 are a result of the device module.

The **beam generation module** creates an extended 3D beam which is build from bundled up quasi-parallel 1D beamlets (see Figure 2.2, left). The beam shape is modelled by applying the appropriate current distribution. Beamlets with no beam current are disregarded [23].

The **observation module** creates an observation profile by which the observation system can be modelled. To create a proper observation profile RENATE has two approaches. The more simplistic approach relies on the camera obscura model [24]. The observation system is reduced to a pinhole

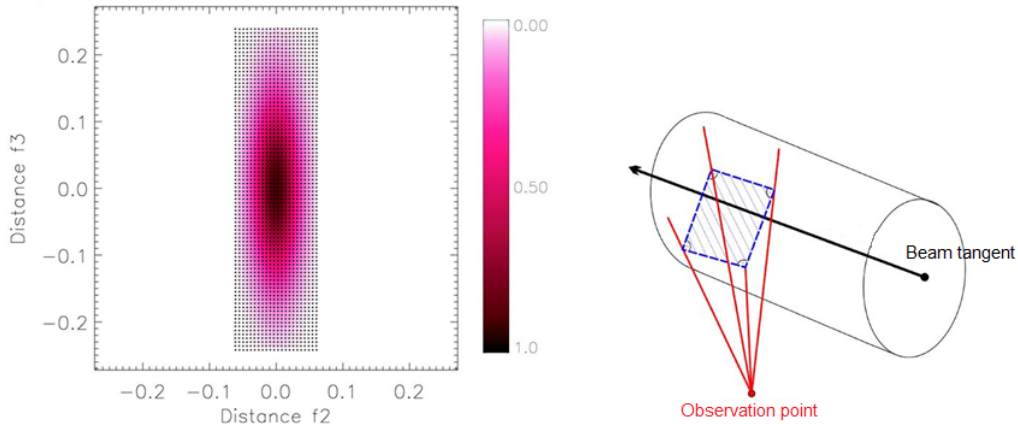


Figure 2.2: *Left: Beam current distribution on a plane perpendicular to beam trajectory. Black dots mark the locations of individual beamlets. Right: Detector pixel projection into the plasma.*

projection system (Figure 2.1) referred to as the observation point, from where quadratic, finite sized detector pixels are projected into the plasma (Figure 2.2, right), creating finite sized regions of interest in the plasma, along the beam. Projecting multiple detector pixels results in an observation profile. A more complicated approach relies on the use of the ZeMax model [25]. The ZeMax model relies on the construction of an optical transmittance matrix for a certain region of interest in the plasma. Light detection from the region of interest in question can be calculated more efficiently for each detector using the transmittance matrix.

The **atomic physics module** contains fits of the collisional cross-sections for certain beam types at the required energies. With the right cross-sections it determines the rate coefficients Equation (1.5) for each reaction type [26]. The rate coefficients are regarding neutral atom collisions with electrons, protons and impurities, calculating collisional excitation, de-excitation and ionization coefficients. Charge exchange rate coefficients are also calculated as well as spontaneous de-excitation events.

The **beam evolution module** calculates the time dependent rate equations for all available beamlets, to determine the electron population along the beam for the monitored atomic levels [8]. Equation (2.1) describes the neutral atom interaction with electrons:

$$\begin{aligned}
 C_{ei} = & -n_i \left(\sum_{j=i+1}^m R_e^{ex}(i \rightarrow j) + \sum_{j=1}^{i-1} R_e^{dex}(i \rightarrow j) + R_e^{ion}(i \rightarrow +) \right) \\
 & + \left(\sum_{j=1}^{i-1} n_j R_e^{ex}(j \rightarrow i) + \sum_{j=i+1}^m n_j R_e^{dex}(j \rightarrow i) \right)
 \end{aligned} \tag{2.1}$$

The first part in equation Equation (2.1) gives the electron loss rate from energy level i by collisional excitation, de-excitation and ionization, where n_i is the electron population on energy level i . The second part of Equation (2.1) gives the electron gain rate on energy level i , through collisional excitation from a lower level and collisional de-excitation from a higher energy level. Equation (2.2) describes neutral atom interaction with ions:

$$\begin{aligned}
 C_{Ii} = & -n_i \left(\sum_{j=i+1}^m R_I^{ex}(i \rightarrow j) + \sum_{j=1}^{i-1} R_I^{dex}(i \rightarrow j) + R_I^{ion}(i \rightarrow +) + R_I^{CX}(i \rightarrow +) \right) \\
 & + \left(\sum_{j=1}^{i-1} n_j R_I^{ex}(j \rightarrow i) + \sum_{j=i+1}^m n_j R_I^{dex}(j \rightarrow i) \right)
 \end{aligned} \tag{2.2}$$

Equation (2.2) is similar to Equation (2.1) with the difference that in the electron loss section of Equation (2.2) rate coefficients for charge exchange have been included. Equation (2.3) describes spontaneous transitions that occur along the beam:

$$C_{Si} = \sum_{j=i+1}^m n_j A(j \rightarrow i) - n_i \sum_{j=1}^{i-1} A(i \rightarrow j) \tag{2.3}$$

Combining Equation (2.1) - (2.3), the electron population on the i energy level is determined by the following equation:

$$\frac{dn_i}{dt} = n_e C_{ei} + \sum_I n_I C_{Ii} + C_{Si} \tag{2.4}$$

Equation (2.4) is a system of equations that calculates the electron population along the beam for all monitored energy levels, where $i = 0, 1, 2, \dots$. The reduced rate equation system is derived from Equation (2.4) by using the assumption that the plasma is scarcely contaminated, furthermore by compensating with beam velocity the equations are transformed from time

dependent to a location dependent differential equation system [8, 23]. The RENATE simulation tool uses three solvers to calculate the electron population evolution along the beam. Electron population calculation is being carried out on all monitored levels. For D and H there are 6 monitored levels, for Li there are 9 and for Na there are 8.

The **light detection module** calculates the amount of detected photon current on each detector upon completion of the beam evolution calculation. It uses the detector pixel projections laid out by the observation profile. It connects the observation point with the edges of the projected detector pixel, realising so called observation cones, as seen in Figure 2.2 right. At the intersection of an observation cone with the beam, all emission values are summed up, thus realizing the detected photon current on one detector [26].

2.1.1 Spatial resolution calculation

The RENATE simulation tool utilises various methods for spatial resolution calculation. The most accurate method is based of fluctuation response calculation. Upon calculation of the detected photon current on each detector, narrow Gaussian type of density perturbations are placed into the plasma along the beam, while the detected photon current calculation is redone for each perturbation individually. The variations in detected photon current are measured for each detector, the response matrix is globally normalized to the highest detector current value. The spatial resolution obtained by the fluctuation response matrix contains the detector size, the geometrical contribution to the spatial resolution as well as the contribution from the emission smearing due to the beam velocity [3, 27].

The **geometrical point spread** module calculates the geometrical contribution to the spatial resolution [28]. The spatial resolution contribution is strongly effected by the alignment of the lines of sight with respect to the magnetic field lines [29, 30]. The stronger the misalignment of the LOS with the magnetic field lines the greater the contribution to the spatial resolution, resulting in its degradation. The lines of sight crossing through the beam are lit up accordingly to the emission values, the emission values along the LOS are projected onto a chosen projection plane by following the magnetic field line. The resulting smear by the projected emission onto the projection plane for a line of sight gives the geometrical spatial resolution.

Furthermore the RENATE simulation tool calculates the contribution to the spatial resolution of the emission smear separately. The calculation is achieved by determining the decay time of the relevant excited atomic level factoring in the local plasma density and taking into account the beam velocity. The obtained value characterises the amount by which the emission

is smeared in beam direction and the impact it has on the spatial resolution [3].

2.2 JT-60SA NBI systems

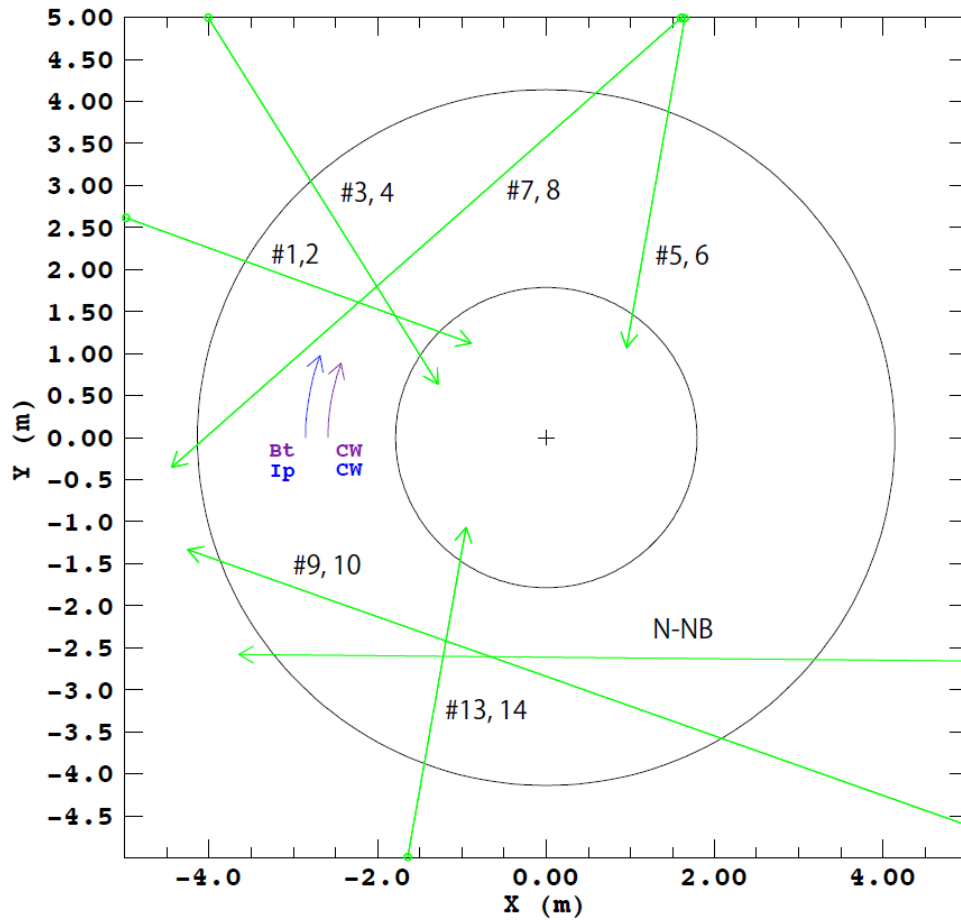


Figure 2.3: Shows a toroidal cross-section of the JT-60SA tokamak in Cartesian coordinate system, $O_{(0,0,0)}$ being the center of the a device. Marked with green are the directions of the NBI beams, while toroidal magnetic field and plasma current directions are marked as well with purple, respectively blue.

The JT-60SA superconducting tokamak is to be equipped with a Deuterium BES (Beam Emission Spectroscopy) diagnostic system. A concept of this system is being developed by the Wigner Research Centre for Physics, aided by BME NTI (Budapest University of Technology and Economics, Department of Nuclear Techniques). My task was to determine the possible

locations for optimal observation in order to have the best spatial resolution possible for the future JT-60SA DBES diagnostic system.

The JT-60SA tokamak is to be equipped with 14 NBI heating beams, which all have the potential of becoming DBES diagnostics as well. Figure 2.3 shows the NBI beams on a toroidal cross-section of the JT60-SA tokamak. Of the 14 beams to be installed, beams #1, #2, #3, #4, #5, #6, #13 and #14 are injected perpendicularly into the plasma, whereas beams #7, #8, #9 and #10 are shot tangentially into the plasma. The device is equipped with two negative ion source N-NBI systems as well. As noticed in Figure 2.3, all NBI beams are presented in pairs, by the same line. Both beams have the same coordinates on the XY plane, however have different starting points in regard to the mid plane [31].

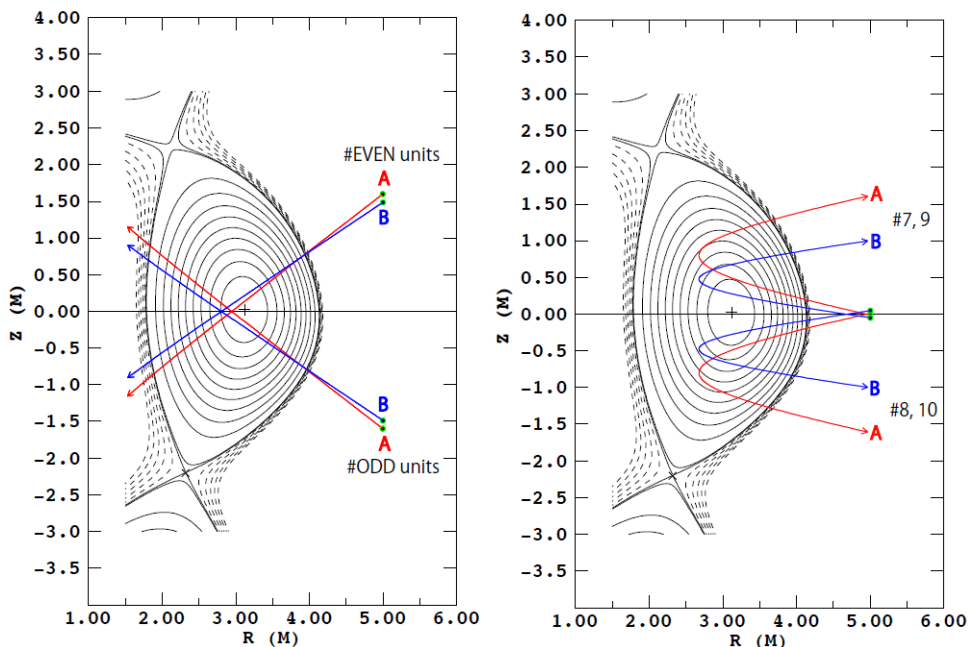


Figure 2.4: Poloidal cross-section of the JT60-SA tokamak, showing the perpendicular beam projection on the left and tangential beam projection on the right, onto a poloidal plane for beam scenarios A (red) and B (blue). Green marks the starting point of the beams.

Each NBI beam has two sources making up for a total 8 tangential beam scenarios (T-NBI) as well as 16 perpendicular beam scenarios (P-NBI). The N-NBI system has two beams, denoted upper and lower beam, depending on the beam source with regard to the equatorial plane. Figure 2.4 shows on the right side the two beam scenarios for the upper perpendicular beam and for the lower perpendicular beam as well as the beam scenarios for the

tangential NBI beams. Red marks scenario A which has a steeper entrance angle to the plasma, while scenario B has a less steep entrance angle. The projection is located on the poloidal plane of the entrance point. Table ?? provides information regarding the output as well as the dimensions of the NBI beams to be installed on JT-60SA [32, 33].

Table 2.1: *NBI parameters*

Data	N-NBI	T-NBI	P-NBI
Beam energy(keV)	500	85	85
Beam power(MW)	5	2	2
Beam height(cm)	13	22	17.5
Beam width (cm)	13.5	24	18.5
Beam divergence(deg)	0.285	1	1

The RENATE simulation code could not provide me with the necessary tools to adequately determine the suitable locations for the DBES diagnostics to be installed on JT-60SA. In order to complete the task, I had to develop a new module for the simulation code. The software development, simulations and results are summed up in Chapter 3 and Chapter 4 assesses the results provided by the newly written routine in the form of a spatial resolution study.

Chapter 3

Optimal Observation Module

The RENATE simulation tool has the capability to calculate the spatial resolution of beam emission spectroscopy diagnostics by means of the geometric point spread function as presented in subsection 2.1.1, amongst others. The simulation tool however does not provide information regarding the ideal location for an observation system. An ideal location for an observation system constitutes of a position that provides the best possible spatial resolution. In case of the large NBI beams (see Table.3.2), the best spatial resolution is obtained by locations that minimize the geometrical contribution to the spatial resolution. Opposed to beams of smaller dimensions such as lithium or sodium beams, where the emission smearing has the vital contribution. The JT-60SA tokamak is being equipped with 14 NBI beams which have a total of 26 beam scenarios that offer a wide range of possibilities for observation locations. In order to conduct a spatial resolution study on the DBES diagnostic system for the NBI beams, I had to develop a module that calculates the locations of the ideal observation systems. Section.3.1 deals with the development of the new module, Section.3.2 summarizes the application of the newly written module while Section.3.3 offers a few scenarios to be studied in detail based on the simulation results.

3.1 Software development

The **Optimal Observation** module is designed to use the beam velocity, direction and the magnetic geometry in order to calculate the location of the ideal observation points as well as the Doppler shift seen at each observation point, providing the necessary information to adequately suggest ports for observation providing ideal spatial resolution.

3.1.1 Optimal observation points

The routine calculates the locations of the optimal observation points for a number of observed points along the beam, which are arbitrarily given by the user, therefore providing not one ideal location for observation but a multitude of locations to be chosen from depending on the observed portion of the beam. The routine produces two main outputs for this calculation. The quantitative output contains Cartesian coordinates along the beam and a corresponding vector which might be placed into a CATIA model of the tokamak in order to ascertain the exact location of the observation point on the tokamak wall. Qualitatively the routine creates 2D angular map of the observation points on a toroidal surface located around the plasma, which serves as a rough approximation for the inner wall of the device.

The geometrical contribution of the spatial resolution is strongly dependent on the angle between the lines of sight and the magnetic field lines. Ideally the lines of sight in the observed region of the beam have to be parallel with the magnetic field lines [28]. Any observation system is expected to be focused on the beam center, therefore the 3D neutral beam is approximated by a 1D beamlet which marks the beam center. A 1D beam evolution is completed with the given beam and plasma parameters calculating the locations of the potentially observed points along the beam as well as the corresponding emission values. On completion of the beam evolution calculation, the normalized magnetic field vectors are calculated for each observed point. In order to have the best possible geometrical resolution, the line of sight vectors are associated with the normalized magnetic field vectors for each point in question. The quantitative output is realized at this point. To have a deeper understanding of the data, qualitative outputs are generated by calculating the intersection of the line of sight vectors with the surface of a torus.

The torus is elliptically shaped and contains the plasma. Torus parameters, as in the major radius of the torus and the minor radii of the ellipse, can be provided as input data by the user, if that is not the case, the torus parameters are calculated from the available magnetic geometry and density profile. The torus' major radius is considered to be the radial distance between the device center and flux surface $\psi = 0$, the plasma center. The ellipses minor and major radii (a and b) are determined by calculating the distance of the plasma center to a given flux surface in radial and vertical directions, respectively.

$$\frac{z^2}{b^2} + \frac{(\sqrt{x^2 + y^2} + R)^2}{a^2} - 1 = 0 \quad (3.1)$$

Equation (3.1) gives the implicit formula for the torus surface, where R is the major radius, a and b are minor and major radii of the poloidal ellipse. At this point the routine calculates the intersections of the LOS with the torus surface and returns two sets of Cartesian coordinates. For any line drawn to a point within the torus there are 2 – 4 intersection points depending on the direction. Terminating the LOS at the first intersection in both directions results in 2 intersection points for every observed point along the beam, which are the locations for optimal observation points.

$$x(\phi, \theta) = (R + a \cos \theta) \cos \phi \quad (3.2)$$

$$y(\phi, \theta) = (R + a \cos \theta) \sin \phi \quad (3.3)$$

$$z(\phi, \theta) = b \sin \theta \quad (3.4)$$

Given the parametric equations for the torus surface, eq.(3.2)-(3.4), the angular coordinates ϕ and θ are determined for each potential observation point, ϕ marks the toroidal angle and θ the poloidal angle.

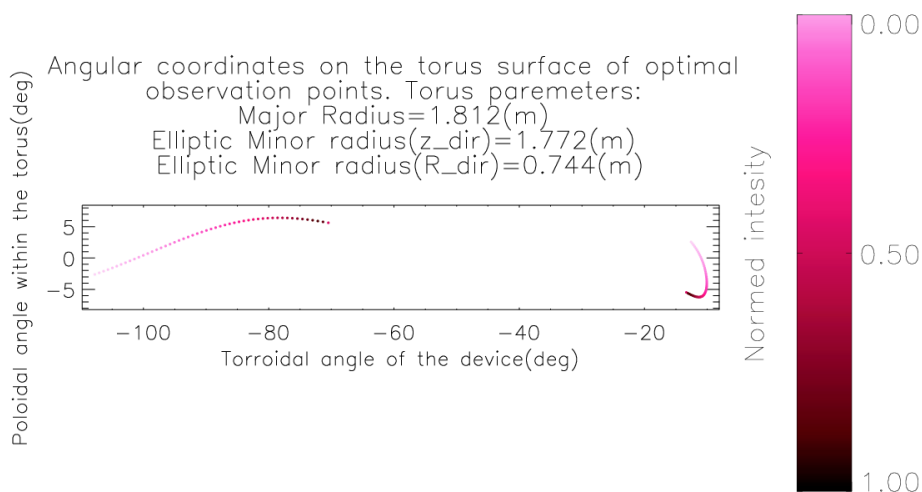


Figure 3.1: *Locations of the observation points location on the torus surface.*

Figure 3.1 shows a 2D representation of the torus surface. The x -axis marks the toroidal angle of the device, where $\phi = 0^\circ$ direction corresponds to the positive direction of the x -axis. The y -axis marks the angle of a point located in the poloidal plane, which is defined by the toroidal angle, with respect to the plasma center. The points presented on the plot correspond to the locations of observation points on the torus surface for the best possible spatial resolution. Purple marks the normalized emission values of the

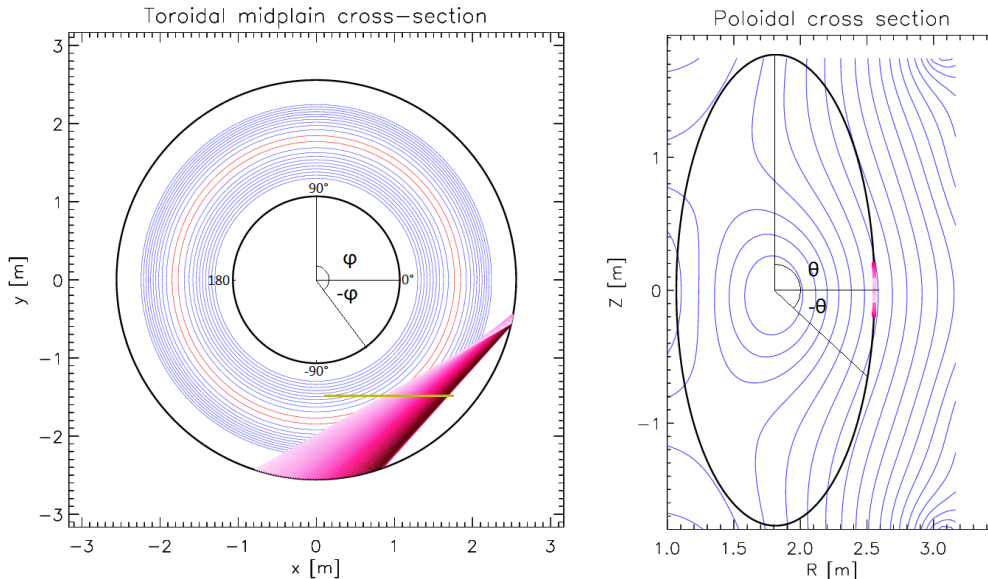


Figure 3.2: *Left image is an equatorial cross-section of the device with the 1D beam plotted with yellow and the lines of sight and their corresponding observation points colour-coded with emission values in purple. Right image shows a poloidal cross-section with the optimal observation points.*

observed point along the beam evolution. Black marks observation points focused on areas of maximal light emission.

Figure 3.2 provides a better understanding of the 2D angular coordinate system. The image on the left side shows the equatorial cross-section of the device. The concentric black circles show the torus surfaces in the cross-section. The 1D beam is plotted with yellow, while the lines of sight and their intersections on the torus surface are plotted with purple with regard to the emission values. The dark purple lines correspond to LOS observing high emission portions of the beam. The image explains the values for ϕ . The image on the right side shows a poloidal cross-section of the imaginary torus (black ellipse). The ideal observation points are colour-coded with regard to the emission of the regions of the beam they observe. The image also explains the values for θ .

3.1.2 Doppler shift

The beam direction with regard to the LOS causes a Doppler shift in the spectrum of the observed light. In case of DBES diagnostics it is of critical importance to find a location for the observation system where the detected light from the beam is clearly differentiable from both the edge D_{alpha} emis-

sion and the C-II line. The D_α line emits at $\lambda = 656.1 \text{ nm}$, which is Doppler shifted depending on beam velocity as well as the angle of the LOS with the beam direction. The C-II line emits at $\lambda = 658.3 \text{ nm}$ [34].

The Doppler shift is calculated by using eq.(3.5), where λ_0 marks the D_α emission, \mathbf{v} marks the beam velocity vector, \mathbf{s} marks the normalized LOS vector and c the speed of light [35].

$$\delta\lambda = \lambda_0 \frac{v}{c} \cos\left(\frac{\mathbf{v}}{v} \cdot \mathbf{s}\right) \quad (3.5)$$

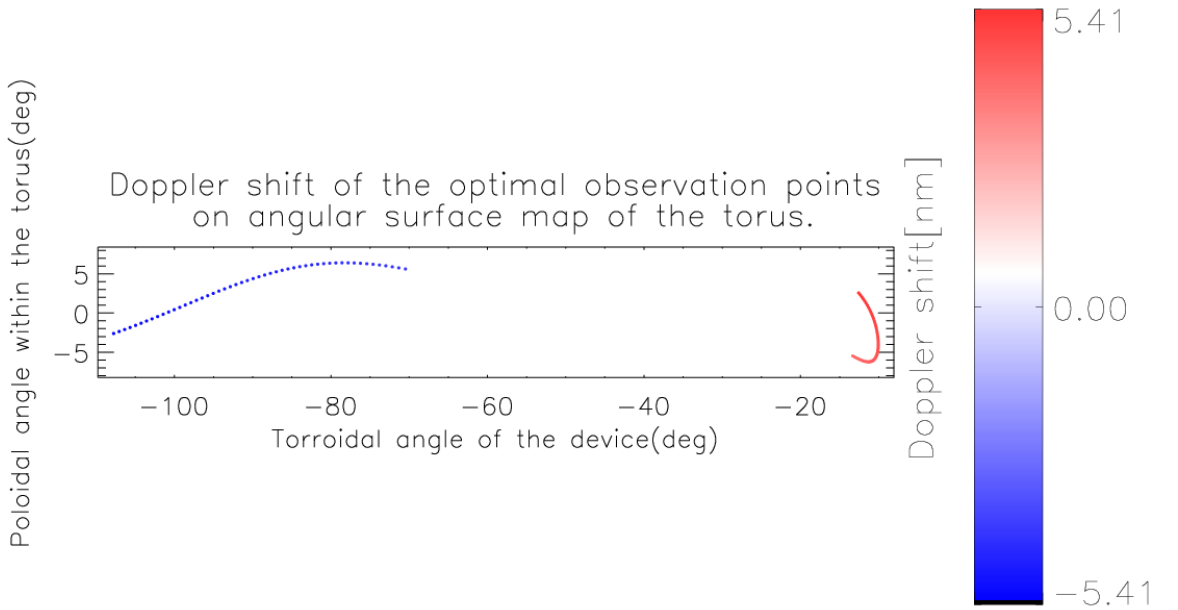


Figure 3.3: Doppler shift for the optimal observation points on the torus surface.

Figure 3.3 shows the 2D angular map as seen in Figure 3.1, the color-coding on this output corresponds with the Doppler shift for each observation point. Blue marks the shift to higher frequencies while red to lower frequencies. The intensity of each color type marks the magnitude of the shift, white meaning no shift at all.

Figure 3.4 shows exactly the amount of Doppler shift to be expected in both lower and higher frequencies for each observed point along the beam. These outputs provide valuable data regarding the omission of the C-II line as well as for spectral filter design. The green shows the D_α line, while purple marks the C-II line.

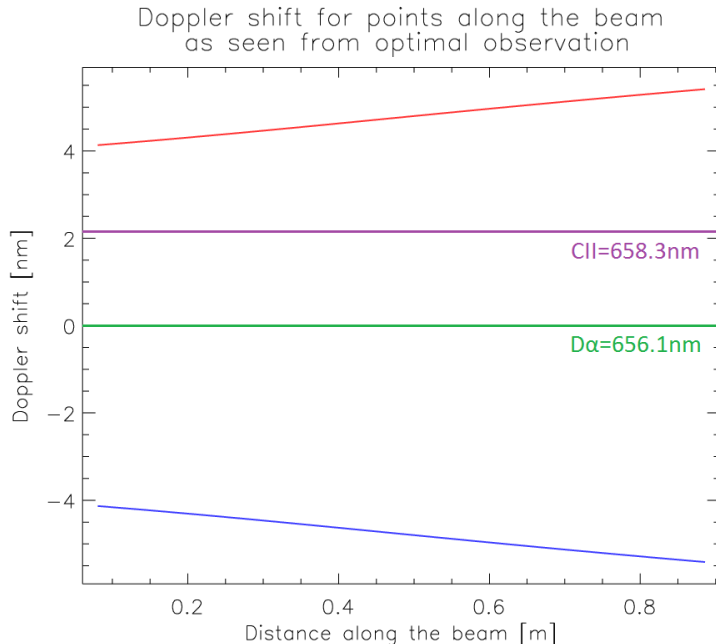


Figure 3.4: Doppler shift values for each observed point along the beam, for both red and blue.

3.2 Simulations on the JT-60SA NBI systems

The JT-60SA tokamak is to be equipped with three different types of NBI beams, as seen in Section.2.2. Most suitable beams are the co- and counter-tangential beams, by providing very favourable viewing positions, as well as the N-NBI beams, however the high beam energy accounts for a considerable smearing along the beam for the latter. The perpendicular NBI beams have been excluded from the study. By definition the perpendicular beams are shot into the plasma close perpendicularly to the magnetic field lines, thus requiring the LOS to be close to perpendicular to the beam direction, therefore disabling the Doppler shift. Studies have been performed on counter-tangential beams on port P-16, co-tangential beams on port P-4 and N-NBI beams on port P-3.

3.2.1 Simulation data

Torus parameters for the simulations have been calculated from the available magnetic geometry and is considered elliptical, as seen in Table 3.1.

All simulations have been carried out using density, temperature and magnetic data provided for **Scenario 5**, which is a non inductive high β

Table 3.1: *Torus data*

Major Radius(m)	3.35
Minor Radius(z direction)(m)	2.7
Minor Radius(R direction)(m)	0.8

plasma scenario [31]. Figure 3.5 shows the plasma density profile as well as the plasma temperature profile for the scenario in question. Both profiles are plotted as a function of the flux surface label, 1 marking the separatrix and 0 the plasma center. The plasma density (left image) has a reasonably smaller pedestal at the plasma edge, and the peak value of $6.77 \times 10^{19} \text{ m}^{-3}$. The density profile registers a considerable increase inside of the pedestal region. The plasma temperature (right image) increases rather more dramatically after the pedestal region from 1 keV to approximately 6 keV. The average plasma impurity charge was set to 6, while the average $Z_{eff} = 2$.

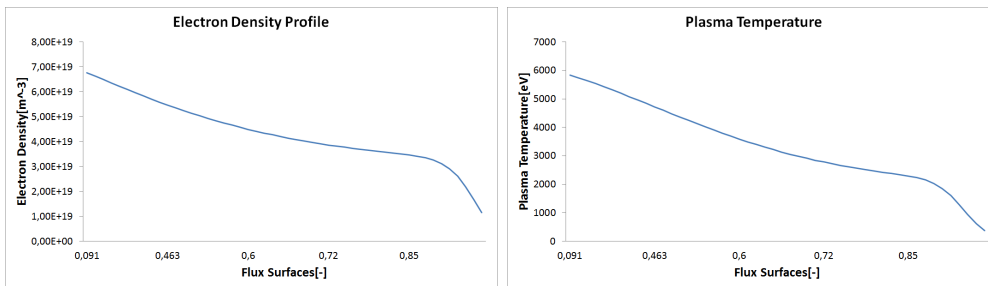


Figure 3.5: *Left image shows the plasma density within the separatrix in function of the flux surface label. Right image shows the plasma temperature within the separatrix in function of the flux surface label. Both images regard Scenario 5.*

Tangential beams offer better observation than their radial counter parts as well as a preferable alignment of the lines of sight with the magnetic field lines. For potential DBES diagnostics tangential beams as well as the N-NBI have been chosen.

Table 3.2: *Beam parameters*

Beam	Beam startpoint(m,m,m)	Beam endpoint(m,m,m)	Port
Beam #7A	0.608, 4.114, 0.189	-0.862, 2.813, 0.567	P-16
Beam #7B	0.649, 4.151, 0.074	-0.390, 3.231, 0.247	P-16
Beam #8A	0.608, 4.114, -0.189	-0.862, 2.813, -0.567	P-16
Beam #8B	0.649, 4.151, -0.074	-0.390, 3.231, -0.247	P-16
Beam #9A	2.382, -3.684, 0.132	0.994, -3.192, 0.415	P-4
Beam #9B	2.064, -3.572, 0.086	0.661, -3.075, 0.271	P-4
Beam #10A	2.382, -3.684, -0.132	0.994, -3.192, -0.415	P-4
Beam #10B	2.064, -3.572, -0.086	0.661, -3.075, -0.271	P-4
N-NBI Upper	2.996, -2.639, -0.598	-0.998, -2.604, -0.79	P-3
N-NBI Lower	2.996, -2.639, -0.501	-0.998, -2.604, -0.309	P-3

The tangential NBI beams are located on ports P-4 and P-16. The N-NBI system is located on port P-3. Star and end points for beam modelling can be seen in [Table.3.2](#).

3.2.2 NBI beams #7 and #8

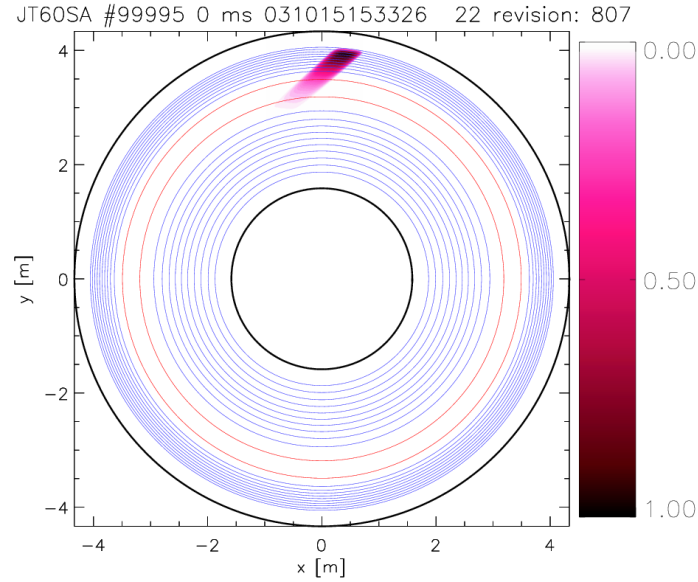


Figure 3.6: *Equatorial cross-section of the device. Blue marks the toroidal magnetic field and the neutral beam is marked with various shades of purple in function of the normalized light emission.*

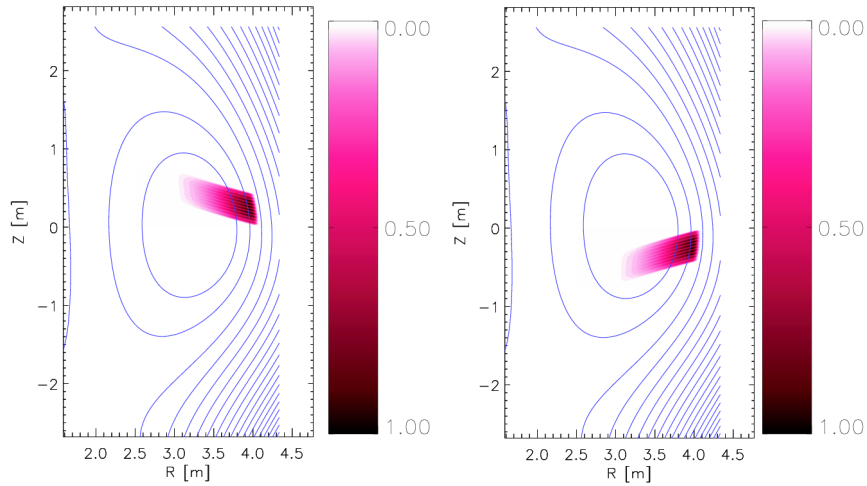


Figure 3.7: *Poloidal cross-section of the tokamak. Blue marks the toroidal magnetic field and the neutral beam is marked with various shades of purple in function of the normalized light emission. Left image shows beam #7 and right image shows beam #8.*

The counter tangential beams #7 and #8 are located on port P-16. Figure 3.6 shows a toroidal cross-section of the tokamak equatorial plane. The toroidal projection of the beam is marked with purple, in function of the normalized light emission values. Differing only in z coordinates, both upper and lower beams have the same projection on the equatorial plane. Figure 3.7 show the lower(left) as well as the upper(right) beam projections on the same poloidal cross-section. Blue marks the magnetic flux surfaces, while the beam is shown in purple, in the function of the normalized light emission. Simulation data regarding coordinates for the two beams is presented in Table.3.2.

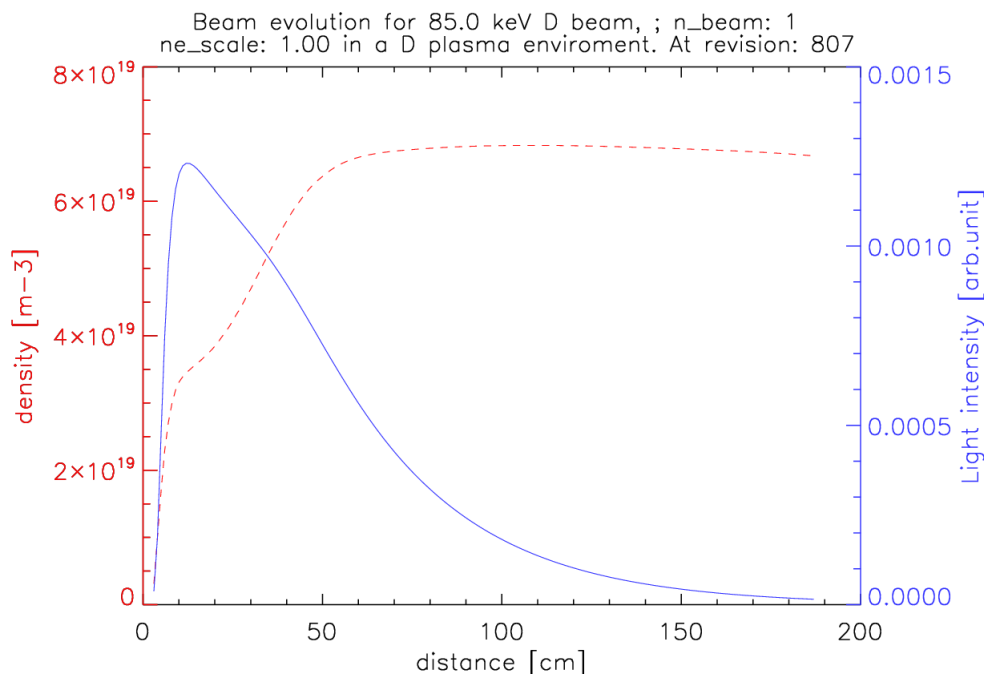


Figure 3.8: *1D beam evolution of an 85 keV deuterium beam shot into a non-inductively driven plasma. The simulated scenario corresponds for beam #7A.*

Figure 3.8 shows the beam evolution of a 1D beamlet corresponding beam #7A, this is the lower counter tangential beam on port P-16, with ion source A. The dotted red line shows the plasma density along the simulated part of the beamlet. The blue line shows the normalized light emission along the beamlet. It is clear that the emission levels drop considerably after 1 m along the beamlet. The highest emission values are recorded in the portion of 10–30 cm along the beamlet, having a peak value at 12 cm along the beamlet. Once the beam hits the denser region of the plasma, at about 50 – 60 cm along the beam with density values of about $6.7 \times 10^{19} m^{-3}$, the emission

values start to drop considerably. Despite the lower emission values in the higher density region of the plasma, corresponding for the plasma center, it is still sufficient for plasma center observations. The 10 – 30 cm region of the beam presents itself to be ideal for pedestal and plasma edge observations. In the inductive current drive mode, the plasma density is expected to increase more dramatically along the beam.

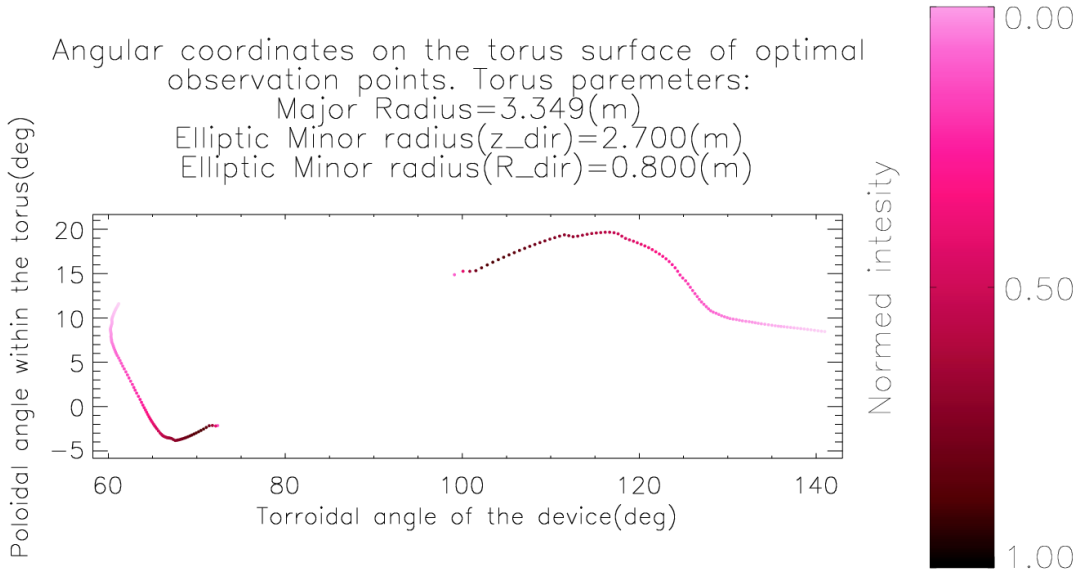


Figure 3.9: Observation points on the torus surface, for optimal spatial resolution on beam #7A. Purple marks the normalized light emission of the observed point along the beam.

Figure 3.9 shows the locations of observation points on the torus surface for optimal spatial resolution for beam #7A. The gap between the two sets of points in the region of $\phi = 85^\circ$ degrees toroidally and $\theta = 7^\circ$ degrees poloidally mark the beam entry point on the torus surface, which corresponds with Figures.3.6 - 3.7 for beam #7A. For observing the high emission part of the beamlet, corresponding to the 10 – 30 cm portion along the beam, two suitable locations have been found. One being located between toroidal angles $\phi = 65 \rightarrow 72^\circ$ and poloidal angles $\theta = -4 \rightarrow -1^\circ$, and one at toroidal angles $\phi = 100 \rightarrow 115^\circ$ and poloidal angles $\theta = 15 \rightarrow 19^\circ$. Due to the extended region observed by the detector array, observation points scattered in a smaller angular range are preferred over observation points scattered in a larger angular range, resulting overall in a more favourable spatial resolution for an extended range of interest. The optimal observation point is located in the vicinity of toroidal angle $\phi = 70^\circ$ and poloidal angle $\theta = -3^\circ$ for beam #7A.

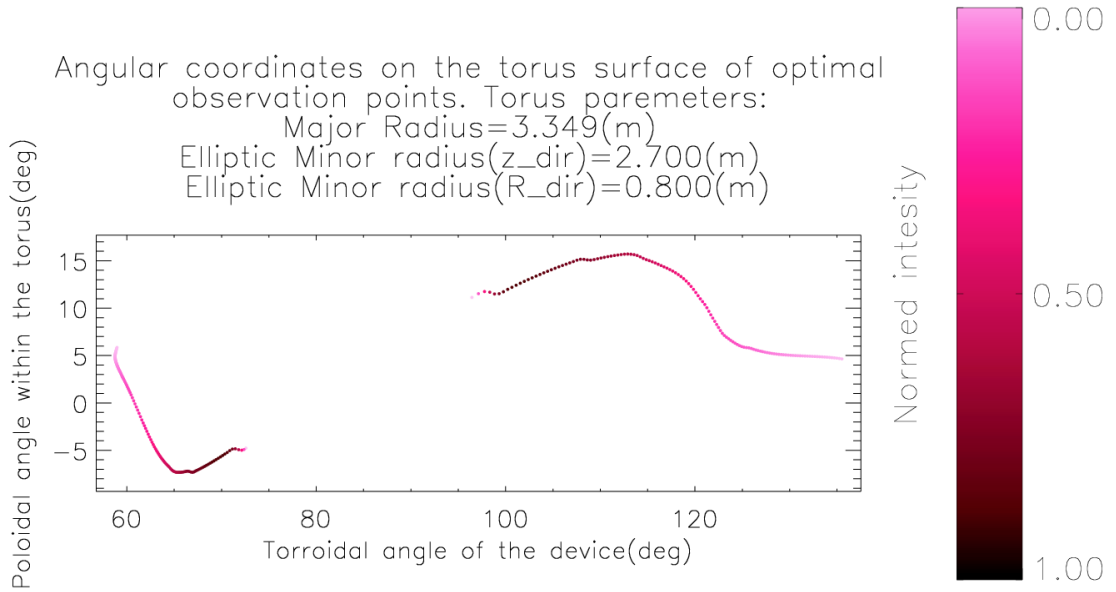


Figure 3.10: Observation points on the torus surface, for optimal spatial resolution on beam #7B. Purple marks the normalized light emission of the observed point along the beam.

Figure 3.10 shows the locations of observation points on the torus surface for optimal spatial resolution on beam #7B. The gap between the two sets of points in the region of $\phi = 85^\circ$ degrees toroidally and $\theta = 4^\circ$ degrees poloidally mark the beam entry point on the torus surface, indicating a slightly lower entry point of the beam. Comparing Figures.3.9 and 3.10, switching the ion source and shooting the beam with a slightly different direction causes the observation point profile to shift with approximately $\delta\theta = 4^\circ$ degrees in the negative direction. The observation point distribution profile suffers negligible variation. The ideal observation point for beam #7B is located at toroidal angle $\phi = 70^\circ$ and poloidal angle $\theta = -8^\circ$ for plasma edge study and toroidal angle $\phi = 63^\circ$ and poloidal angle $\theta = -4^\circ$ for plasma core study.

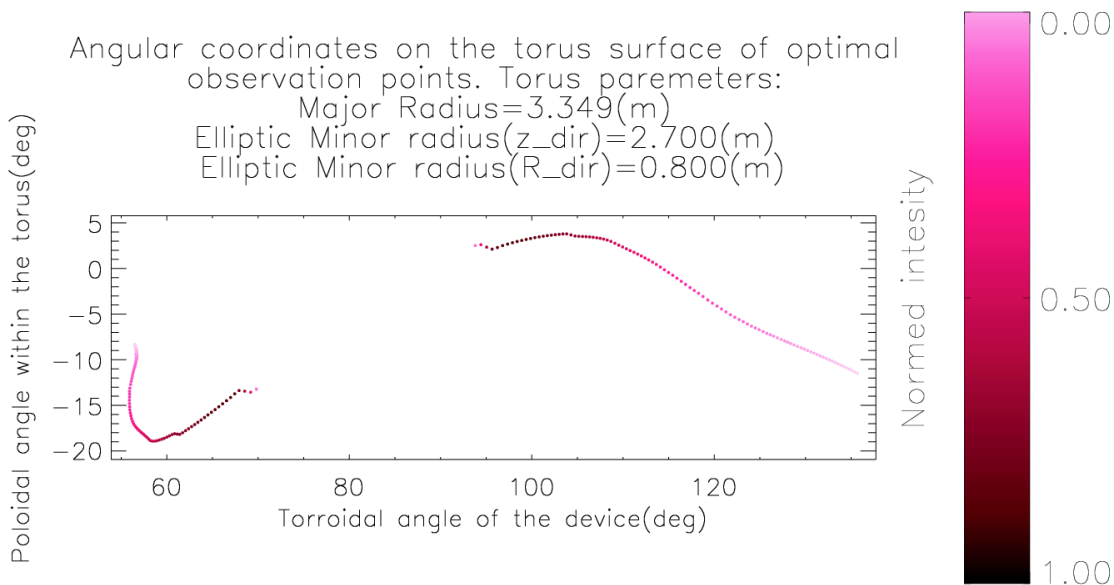


Figure 3.11: Observation points on the torus surface, for optimal spatial resolution on beam #8A. Purple marks the normalized light emission of the observed point along the beam.

Figure 3.11 shows the locations of observation points on the torus surface for optimal spatial resolution on beam #8A. The gap between the two sets of points in the region of $\phi = 83^\circ$ degrees toroidally and $\theta = -5^\circ$ degrees poloidally marks the beam entry point on the torus surface for the upper counter tangential beam on port P-16. Optimal observation point profile for the current scenario is highly similar to the profiles simulated for beams #7A and #7B. The observation profile has shifted poloidally in the negative direction with approximately $\delta\theta = 10^\circ$. The optimal observation point distribution has shifted as well $\delta\phi = 5 - 7^\circ$ in the toroidal direction to $\phi = 62^\circ$. Figures 3.9, 3.10 and 3.11 clearly indicate that there are two possible observation points for the counter tangential NBI beam on port P-16. One is located around $60 \rightarrow 70^\circ$ toroidally, depending on which part of the beam it observes, the other point is located between $100 \rightarrow 120^\circ$ toroidally. The poloidal position of the observation point may vary between $-20 \rightarrow +10^\circ$ or $3 \rightarrow 20^\circ$ depending on the toroidal position and the beam it focuses on. This conclusion is supported by Figure 3.12.

Figure 3.12 shows the equatorial cross-section of the device, where the blue lines mark the toroidal magnetic field lines, while the lines with purple mark the LOS along the beam. The various shades of purple mark the emission values located at the lines of sight. Dark purple marks strong emissions,

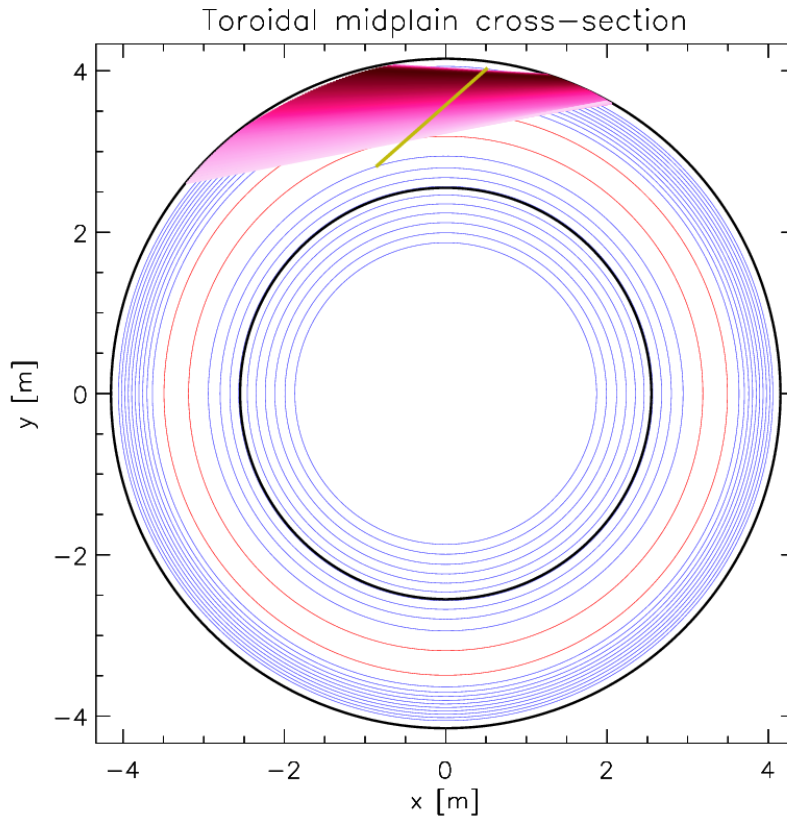


Figure 3.12: *Equatorial cross-section of the device. Blue marks the toroidal magnetic field. The purple lines show the LOS for an ideal observation system.*

while white less so. The yellow line is a 1D representation of the neutral beam. The two concentric black circles mark the torus boundaries used for the simulation. The region located around 70° toroidally offers much more favourable radial resolution over all detectors in respect to the observation region located around 115° toroidally, however there is most likely a trade off between the two locations regarding the poloidal and the radial resolutions.

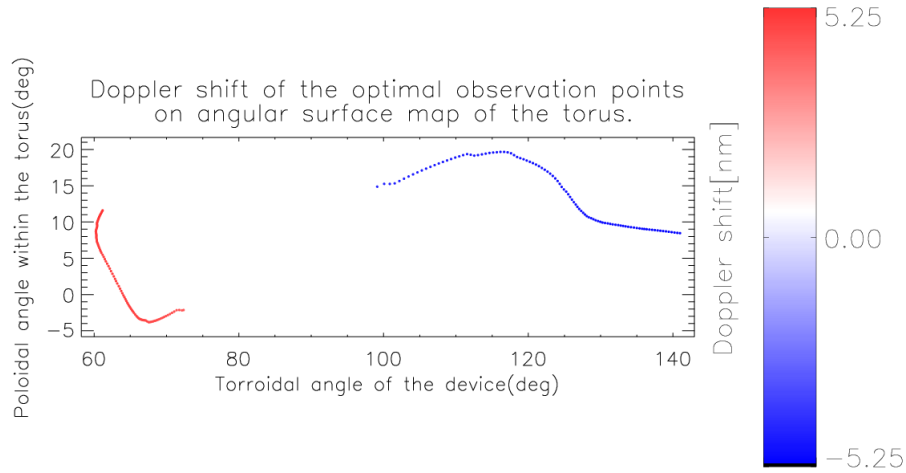


Figure 3.13: Doppler shift detected by each observation point on an angular map of the torus surface of beam #7A.

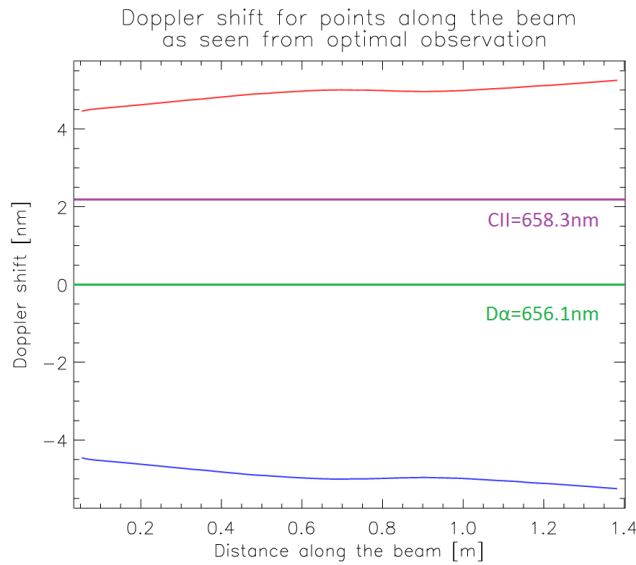


Figure 3.14: Doppler shift detected by each observation point for specifically observed regions along the beam, for beam #7A.

Figure 3.13 shows the Doppler shift for each observation point on beam #7A. Observation points located behind the beam with regard to its direction register a red shift located between $\phi = 60^\circ$ and 75° , while observation points located in front of the beam between $\phi = 100^\circ$ and 140° are shifted blue. The maximal Doppler shift in both directions is of $\delta\lambda = 5.25 \text{ nm}$, well beyond the wavelength of the C-II emission. Figure 3.14 shows that the

Doppler shift gradually increases from the plasma edge at $\delta\lambda = 4.5 \text{ nm}$ to 5.25 nm . The C-II line is shifted with $\delta\lambda = 2.2 \text{ nm}$, marked with purple while D_α line is marked with green. The observation points observing the highest emission portion of the beam, between 10 cm and 30 cm average a Doppler shift of 4.8 nm . Beam #7B shows the the same amount of shift with $\delta\lambda = 4.4 \text{ nm}$ to 5.11 nm , increasing gradually. Beams #8A and #8B however register a far lower value for the plasma edge of 3.1 nm at the plasma edge, averaging at 3.6 nm for the high emission region of the beam. The shift considerably increases towards the plasma center to a value of 5.04 nm . An observation point directed towards either beam #7A or #7B is clearly the safer choice regarding the Doppler shift.

3.2.3 NBI beams #9 and #10

Simulations performed on the co-tangential NBI beams show a similar behaviour as seen for the counter-tangential beams. The toroidal positions of the optimal observation points are similar for all four beam scenarios, a considerable variation arises only in the poloidal positions in the form of an angular shift. Beams #10A, B exhibit the same trend as do beams #7A, B. The same is true for beams #9A, B and #8A, B. Beam #9A is used as a reference scenario in further discussion.

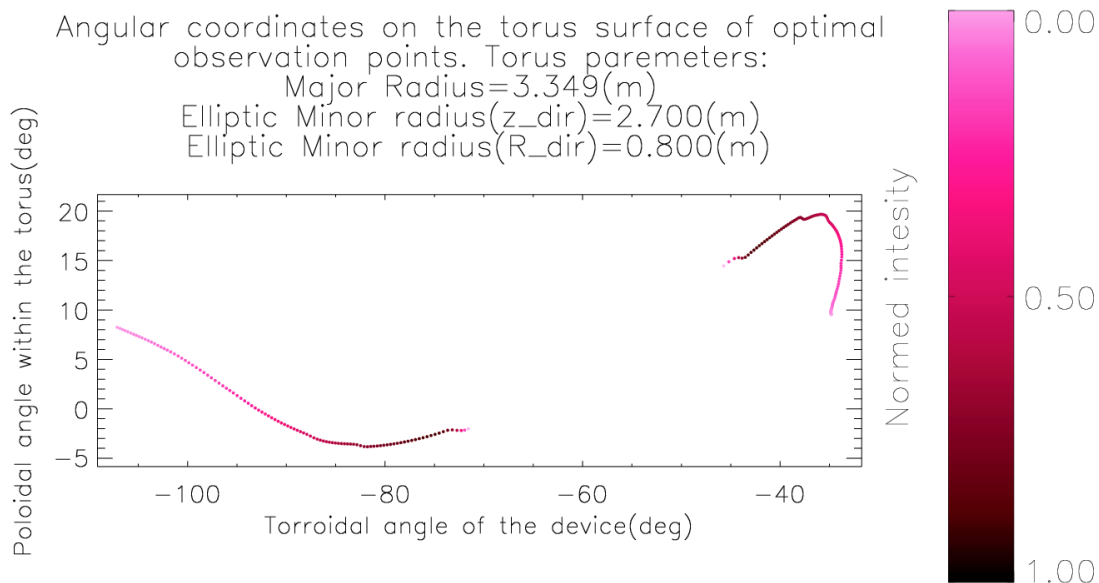


Figure 3.15: Observation points on the torus surface, for optimal spatial resolution on beam #9A. Purple marks the normalized light emission of the observed point along the beam.

Figure 3.15 shows the locations of the optimal observation points on the torus surface. Observation points around the toroidal region of $\phi = -40^\circ$ are scattered over an interval of 10 – 15 degrees for the observation of the entire beam. On the other hand, observation points located in front of the beam, with regard to the beam direction, are scattered over an interval of 30 degrees. An ideal observation point for the high emission region of the beam being located at $\phi = -80^\circ$. The registered poloidal shift between beams #9A and #9B is of $\delta\theta = 5^\circ$ while the shift between the reference scenario and beam #10A is of 14° . In the case of beams #10A, B, the observation points for the plasma interior are scattered over a slightly larger interval suffering a toroidal shift of approximately 5° , this effects only observation points pointed towards portions along the beam at 60 – 80 cm, resulting in an overall poor resolution with respect to beams #9A, B.

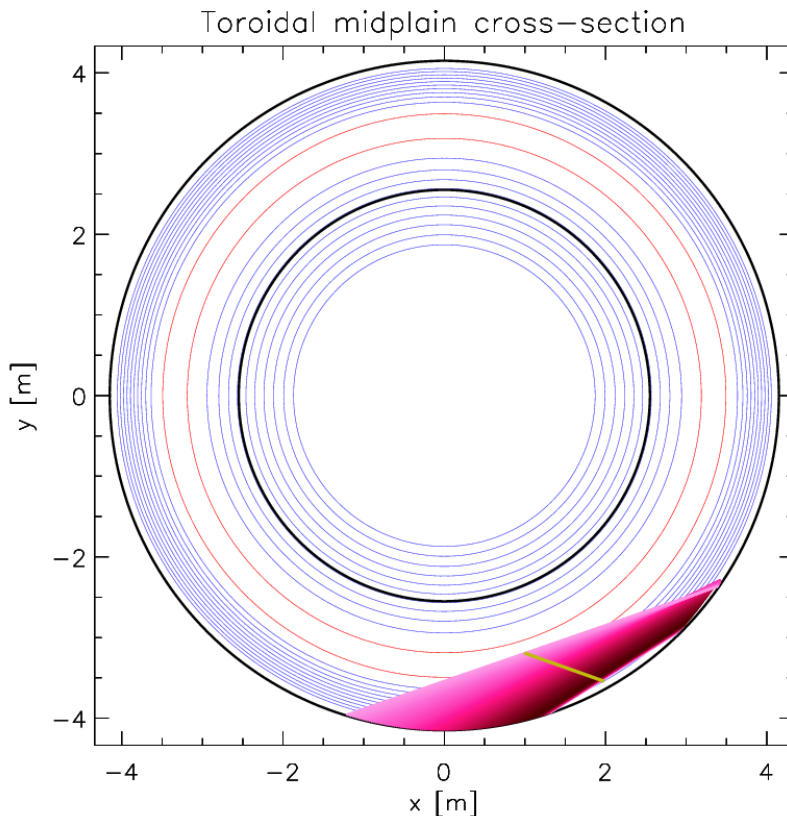


Figure 3.16: *Equatorial cross-section of the device. Blue marks the toroidal magnetic field. The purple lines show the LOS for an ideal observation system.*

Figure 3.16 confirms the finding so far, optimal observation points are located toroidally around $\phi = -40^\circ$ for observation from behind the beam,

while observation points located in front of the beam should be placed toroidally around $\phi = -83^\circ$.

The Doppler shift for the observation points from behind the beam is red and observation points from the front of the beam is blue, as expected.

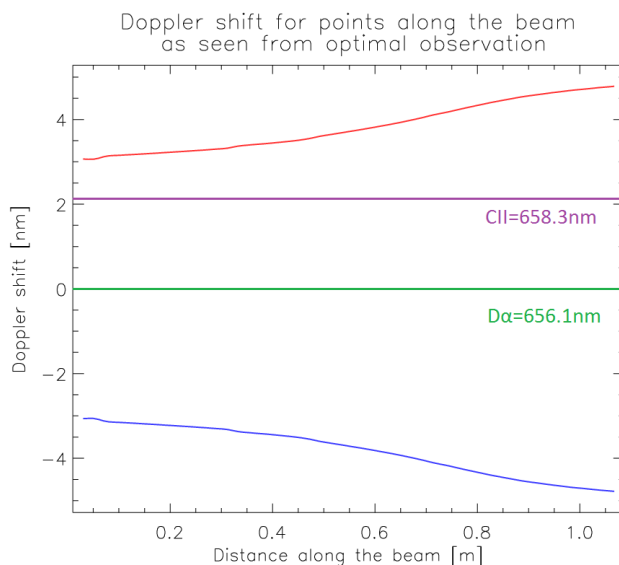


Figure 3.17: Doppler shift detected by each observation point for specifically observed regions along the beam, for beam #9A.

Figure 3.17 shows beam #9A producing a shift of 3.3 nm to 3.7 nm for plasma edge observation. The figure shows the C-II line at 658.3 nm, marked with purple, 2.2 nm towards the red shifted side of the D_α emission. The Doppler shift increases towards the plasma core having a peak value of 4.78 nm. Beam #9B registers surprisingly an increase of 0.3 – 0.4 nm for all observation points resulting and averaged shift of 4 nm for plasma edge observation and having a peak value of 5.2 nm in the plasma interior. The Doppler shift values for beams #10A, B are much higher in the plasma edge, averaging at 4.4 nm and peaking at 5.1 nm in the plasma core.

3.2.4 N-NBI beams

The beam energy of 500 keV pushes the N-NBI beams well across the plasma core resulting in beam emission on the high field side of the device. Figure 3.18 shows the beam evolution of the upper N-NBI beam. The blue line shows the normalized light emission along the beamlet, while the dotted red line the plasma density along the beamlet. The half maximum of light emission is located in the plasma core at 150 cm along the beam. The drop

in plasma density at distance along the beam of 270 *cm* indicates that the beam reached the high field side of the plasma, still having %10 of maximal emission.

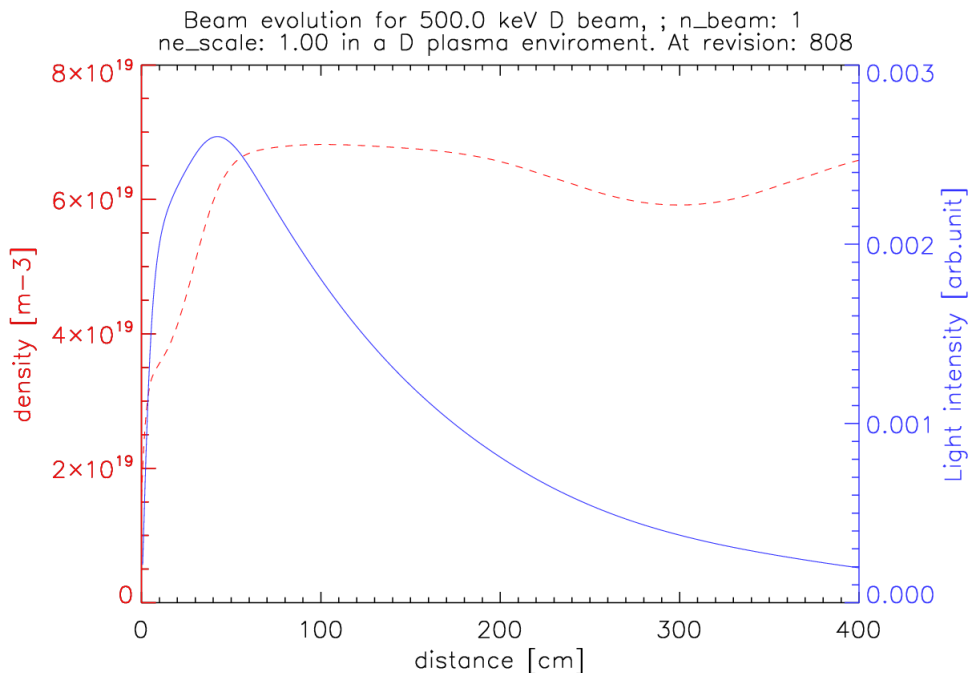


Figure 3.18: 1D beam evolution of a 500 keV deuterium beam shot into a non-inductively driven plasma. The simulated scenario corresponds for the upper N-NBI beam.

Figure 3.19 shows the locations for ideal observation points for the upper N-NBI beam. The upper beam is used as a reference beam and discussed in detail. The lower N-NBI beam exhibits the same behaviour regarding the locations of the observation point, the only significant difference being a poloidal shift of $\delta\theta = 10^\circ$ in the positive direction for the lower N-NBI beam. In case of both observation scenarios, observing the beam from behind or from the front, the ideal observation points are scattered over a large angular interval toroidally. The observation points located behind the beam offer a slightly better overall radial resolution for overvarions focused on the beam edge. The observation points are scattered on the interval poloidally for both observation scenarios. An observation system located at toroidal angle $\phi = -25^\circ$ and poloidal angle of $\theta = -7^\circ$ seems to be the only ideal location for an observation system in the case of the upper N-NBI beam. The lower N-NBI beam displays the same profile with the difference in the ideal position being located at $\theta = 3^\circ$ poloidally.

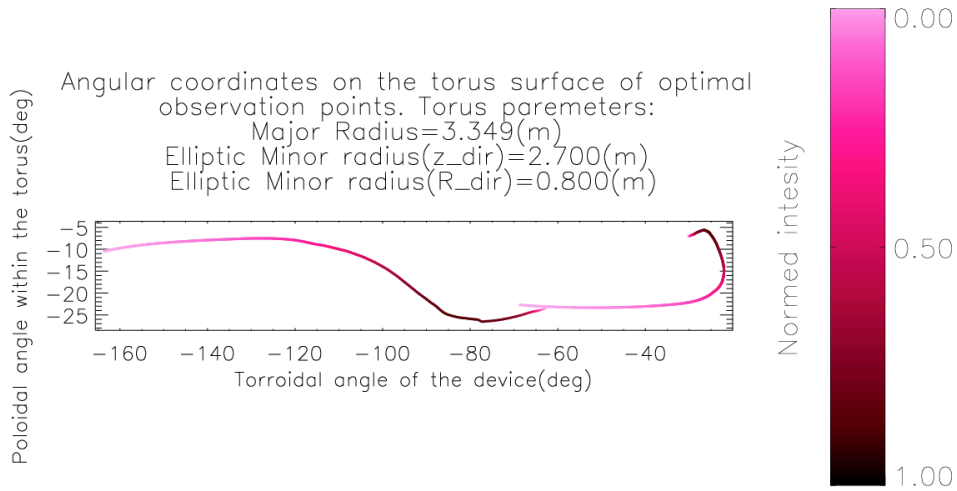


Figure 3.19: Observation points on the torus surface, for optimal spatial resolution on upper N-NBI beam. Purple marks the normalized light emission of the observed point along the beam.

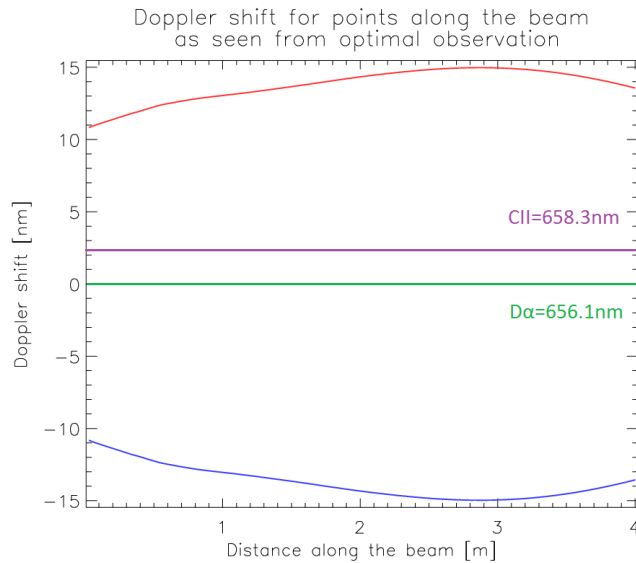


Figure 3.20: Doppler shift detected by each observation point for specifically observed regions along the beam, for upper N-NBI beam.

Figure 3.20 shows the Doppler shift produced by the upper N-NBI beam along the beam for each ideal observation point. The shift at the plasma edge is of 10 nm, as the beam crosses the plasma core, it peaks at 15 nm and slightly drops on the high field side of the plasma. The lower N-NBI beam

exhibits the same behaviour. It is clear that the Doppler shift for the any N-NBI beam observation scenario is far greater than to suffer any interference from the C-II emission, marked with purple at 658.3 nm .

3.3 Recommended scenarios

After careful consideration of the simulation results obtained in Section 3.2 I suggest three possible observation scenarios, one for each beam. For each of these scenarios I have conducted a detailed spatial resolution study discussed in Chapter 4.

Considering only the locations of the observation points, it is clear that there has to be a trade-off in overall poloidal and radial resolution considering observation systems in front of the beam respectively behind the beam. This tendency is obvious from the range of the angular interval at which the observation points are scattered toroidally. Beams #7A, B display a mirroring behaviour with regard to beams #10A, B, considering the Doppler shift as well as the distribution of observation points. The same can be said for the behaviour of the other two beam pairs. Comparing the toroidal distribution of the observation points for beams #7 and #10 with respect to the distribution of beams #8 and #9, it is clear that the former are more suitable for plasma edge observations while the latter for plasma core observations. Though all beam scenarios prove to have sufficiently good overall radial resolution for edge observation, the latter beam pair shows a considerably lower Doppler shift making them less suitable for edge observation. Of course this consideration deserves merit only if observed from behind the beam. For plasma core observations however, observation from behind the beam offers sufficiently favourable overall radial resolution. This is due to the steeper profile in the observation point distribution for points located in the plasma core along the beam. Such is the case of beams #8 and #9 which makes them prime candidates for such studies. The preferred beam in this case is beam #9B producing the largest red shifted Doppler for its observation points, having a Doppler shift of $\delta\lambda = 4.4 \text{ nm}$ which is 2.2 nm more than the C-II peak. In case of the N-NBI beams the Doppler shift is so high that it becomes of no consequence. The trade-off between overall poloidal and radial resolution is negligible, making the edge observation from behind the beam the most viable location for an observation system.

The suggested scenarios for observation systems are as follows:

- **Scenario 1:** Plasma edge observation on counter-tangential beam #7A.
- **Scenario 2:** Plasma core observation on co-tangential beam #9B.

- **Scenario 3:** Plasma edge observation on upper N-NBI beam

Chapter 4

Benchmarking

In light of the simulations performed and discussed in Chapter 3, I had chosen three scenarios to be studied. For each scenario an extended beam calculation has been performed to ascertain the amount of detected light for the proposed observation point. The geometrical point spread module has been used to calculate the radial and poloidal resolutions in order to verify and support the simulations results calculated by the optimal observation module. The emission smear module was used in order to determine the impact the emission smear has on the spatial resolution. For the simulation a 4×16 sized detector grid has been modelled, with a projected detector size of 1 cm on the beam. Figure 4.1 shows the detector projection onto the beam, where the x -axis marks the distance along the beam where the detectors are projected and the y -axis marks the distance of the projections with respect to the beam center, marked with red. The lens radius used for the simulations is of $R = 5$ cm, while the optical transmission rate is set to $\eta = 0.5$.

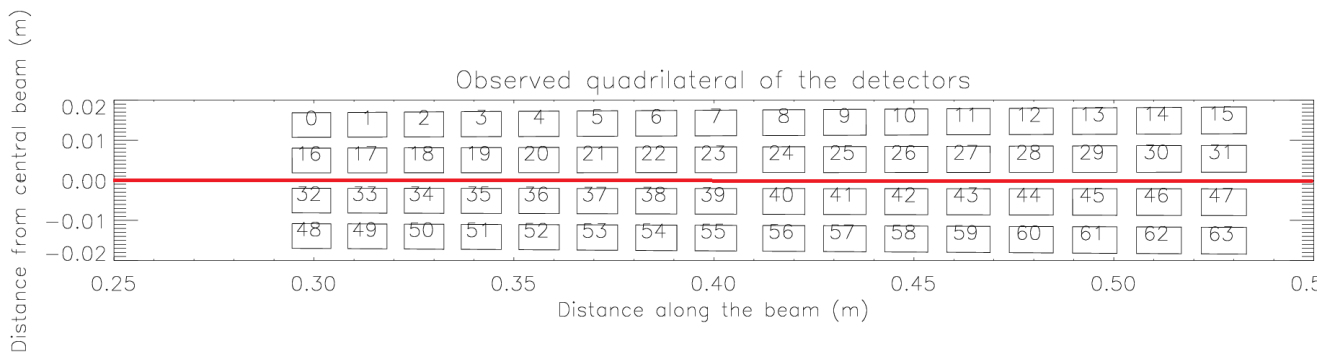


Figure 4.1: *Detector projections onto the beam as seen from the observation point.*

4.1 Plasma edge scenario

For the plasma edge scenario beam #7A was chosen. Simulations have been carried out on both observation points, one being located in front of the beam while the other from behind the beam. The observation system was directed at a 23 cm portion of the beam located between 15 cm to 38 cm along the beam. According to the simulation result from the optimal observation module, the observation point from behind the beam should be located on port P-17 while the observation point from in front of the beam on port P-14, however with the proper port plug and extension, P-15 might be a suitable candidate as well (see Figure 4.2).

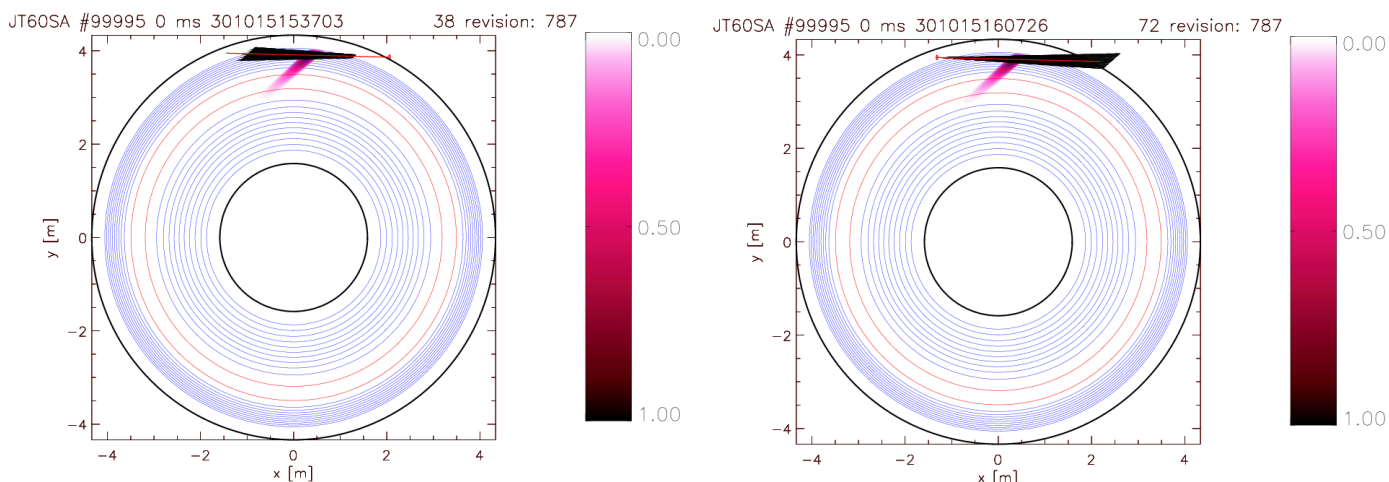


Figure 4.2: *Toroidal cross-section of the device. Left image shows the observation point from behind the beam. Right image shows the observation point from in front of the beam. The LOS for each detector are marked with black, the observation system and viewing direction marked with red.*

Beam evolution studies for both observation systems show roughly the same amount of detected photons for both observation systems. Figure 4.3 shows the detected photon current for both observation systems. The y -axis shows the amount of photons detected, while the x -axis the detector index. Four distinct light profile are observable due to the four detector rows. The upper image shows the light profile for observation behind the beam, the lower image shows the light profile for observation in front of the beam. The maximal detected photon current is of 1.18×10^{11} 1/s for both systems making them both efficient for plasma edge observation. The highest photon current is detected on detector pixel column #3, observing the 20 cm portion along the beam. The amount of detected light slowly drops as the beam penetrates

deeper into the plasma. The observation system behind beam registers a slower drop of detected light towards the plasma center than its counterpart. For the observed region the calculated Doppler shift is between 4.5 nm and 5 nm shifted blue as well as red, therefore making the spatial resolution and port availability the decisive factor in determining the proper location for an observation system. The shift is well beyond the C-II peak located at $+2.2 \text{ nm}$ from the D_α line.

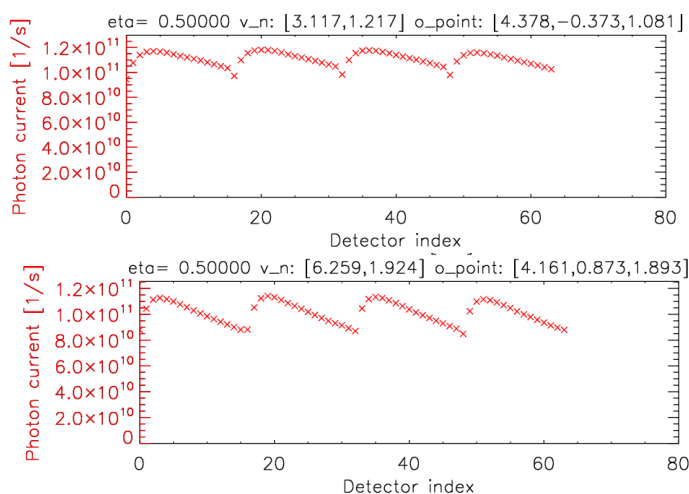


Figure 4.3: Shows the detected photon current for each detector channel. Upper plot show the photon current values for observation behind the beam. Lower plot show the photon current for observation in front of the beam.

Figure 4.4 shows the spatial resolutions for observation in front of the beam. The left image shows the radial resolution which has an average value of 7.43 mm . The "V" shaped profile of the resolution indicates that the detector pixels located in center of the detector array have the best resolution of $1 - 2 \text{ mm}$. This is a direct result of the locations provided by the optimal observation module. The radial resolution degrades for detector pixels located at the ends of the observed region indicating a strong deterioration of radial resolution. The right image shows the poloidal resolution which exhibits similar behaviour, nevertheless having a far more favourable overall resolution. Figure 4.5 shows the spatial resolution for the observation point behind the beam. The left image shows the radial resolution which is overall 4.15 mm and as expected far superior to the observation in front of the beam. The same is to be said about the poloidal resolution, averaged at 2.16 mm . It is clear that the toroidal scattering of the observation point on the blue shifted side of the beam has a far greater impact on the resolution than the scattering of observation points poloidally on the red shifted side of

Spatial resolution calculation for the DBES diagnostics on JT-60SA

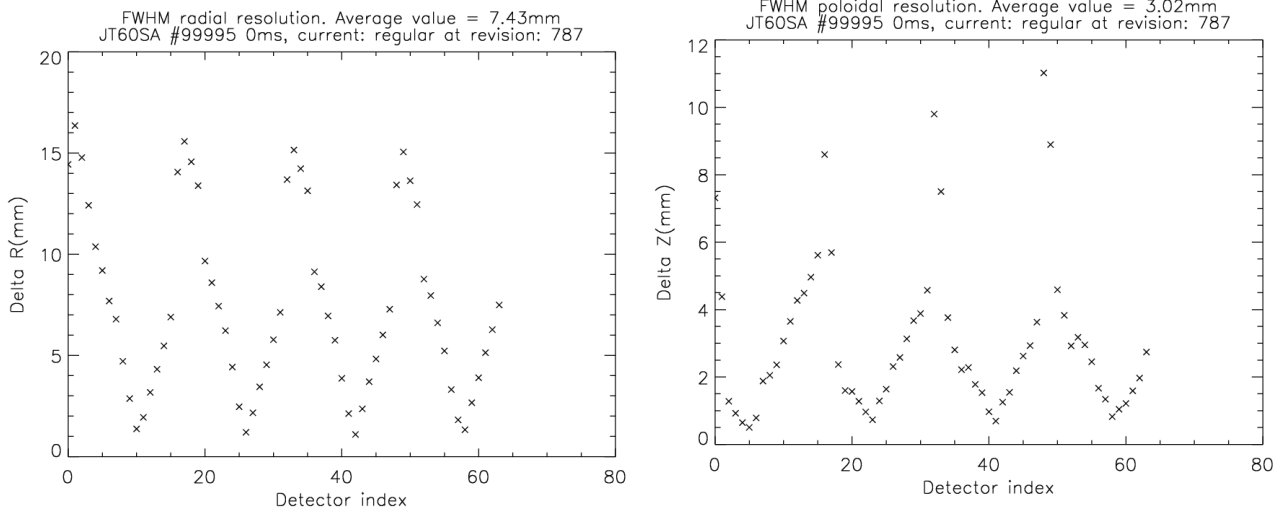


Figure 4.4: *Left image shows the radial resolution for each detector pixel for observation in front of the beam. Right image shows poloidal resolution for observation in front of the beam.*

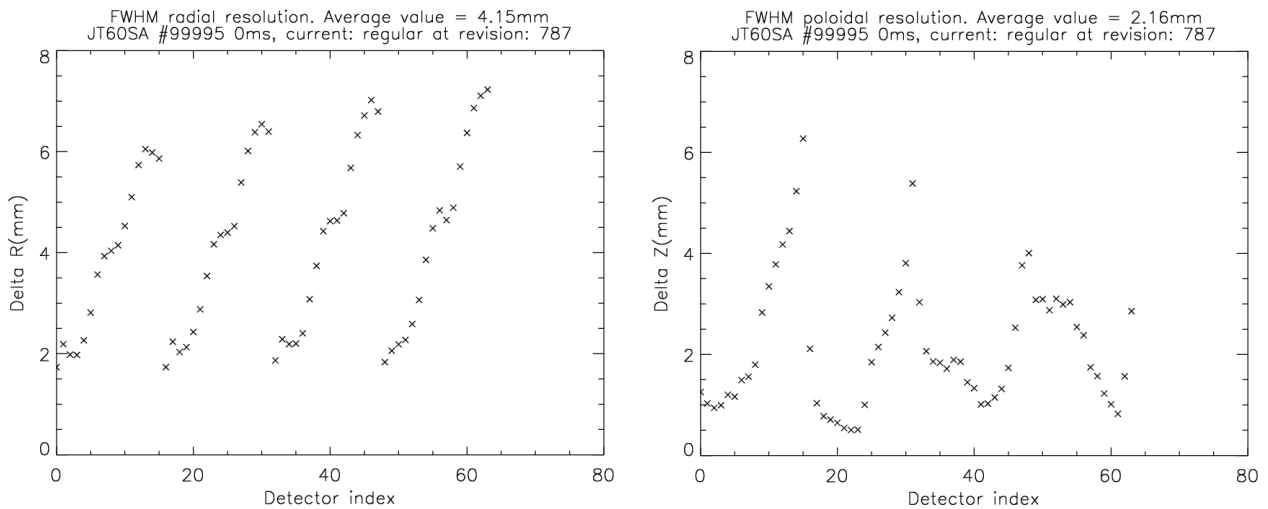


Figure 4.5: *Left image shows the radial resolution for each detector pixel for observation behind the beam. Right image shows poloidal resolution for observation behind the beam.*

the beam. Simulations calculating the contribution of the emission smear to the spatial resolution show an added 5 – 3 mm to the resolution for the red shifted observation system, while a 4 – 3.5 mm addition in the case of the blue shifted observation system. A slight decrease in emission smearing however

does not justify a large increase in geometrical spatial resolution. The spatial resolution study for edge observation scenario on beam #7A conclusively supports the observation point be placed on port P-17.

4.2 Plasma core scenario

The plasma core observation scenario has been simulated on co-tangential beam #9B. In this scenario only one observation point will be discussed, located behind the beam.

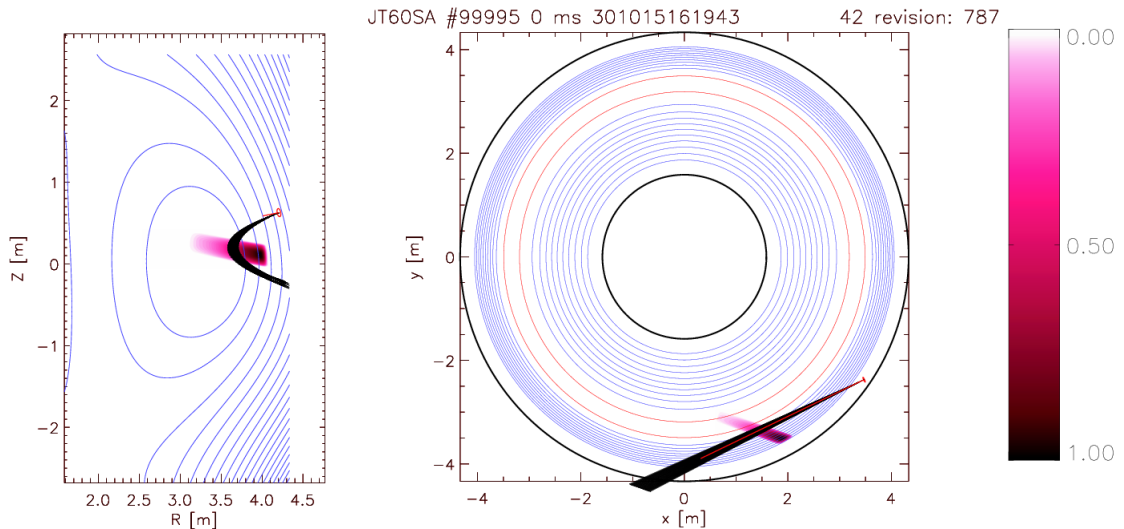


Figure 4.6: *Left image shows the poloidal cross-section. The right image shows the toroidal cross-section. The LOS for each detector are marked with black, the observation system and viewing direction marked with red.*

Figure 4.6 shows the location of the observation point on a toroidal cross-section as well as on a poloidal cross-section. Purple marks the beam emission while the black lines the LOS. The toroidal cross-section shows the observation point ideally placed on port P-3, which houses the N-NBI beams. However the poloidal cross-section places the observation point well above the equatorial mid plane which is favourable considering the N-NBI beams are shot below mid plane into the plasma. The beam evolution calculation performed on the co-tangential beam, with an observed region located between 55 – 78 cm along the beam, for plasma core observations has yielded quite acceptable detected photon current values considering the penetrated depth into the plasma. Figure 4.7 shows the detected photon current on each

detector channel, having a peak value of 2.56×10^{10} 1/s which is steadily declining closer towards the plasma center. The Doppler shift in this region is calculated to be between 3.5 – 4.2 nm, which is close to the C-II line. Moving the observation range deeper into the plasma increases the Doppler shift, however detected photon current values might drop slightly below 10^{10} 1/s. An easy alternative for greater light detection with a deeper observation is the increase in projected detector size.

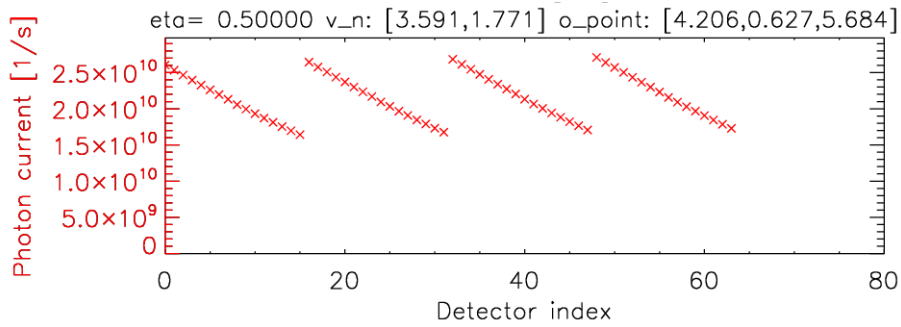


Figure 4.7: Shows the detected photon current for each detector channel.

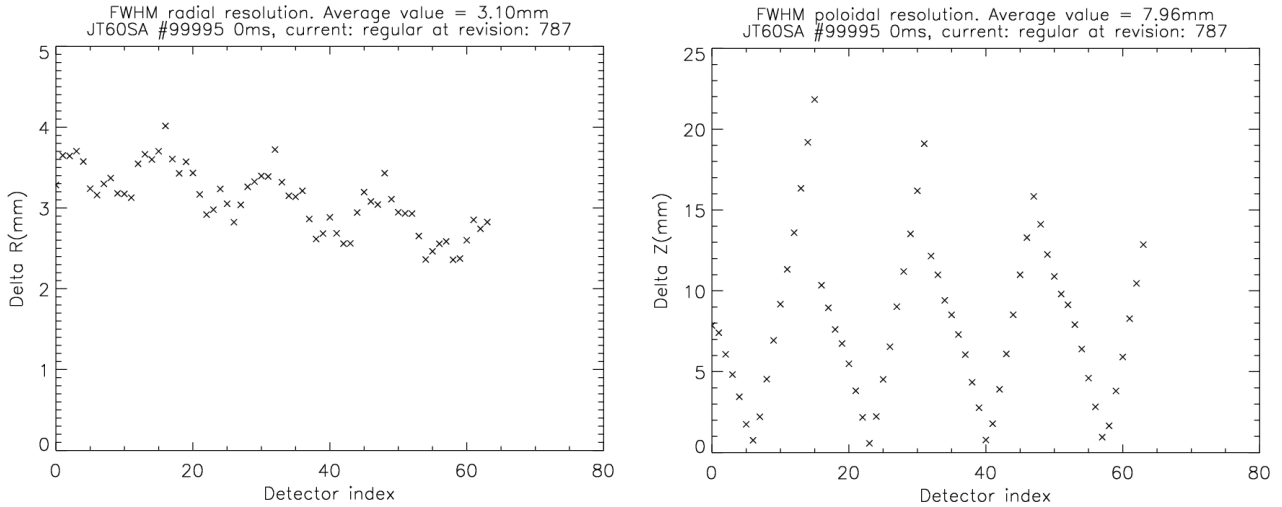


Figure 4.8: Left image shows the radial resolution for each detector pixel for observation behind the beam. Right image shows poloidal resolution for observation behind the beam.

Figure 4.8 shows the radial and poloidal resolutions for the current scenario. As expected the overall radial resolution, averaged at 3.1 mm, is far less degraded than the poloidal resolution, averaged at 7.96 mm. The sheer

amount of degradation at the edges of the observed region along the beam, confirms the predictions of the optimal observation module. Simulations carried out using the emission smear module show an addition to the geometrical resolution of $3.2 - 2.8 \text{ mm}$ decreasing towards the plasma core. The current scenario offers favourable spatial resolution for plasma core observations as well as reasonable light emission.

4.3 N-NBI scenario

Upper N-NBI beam has been chosen for the N-NBI study.

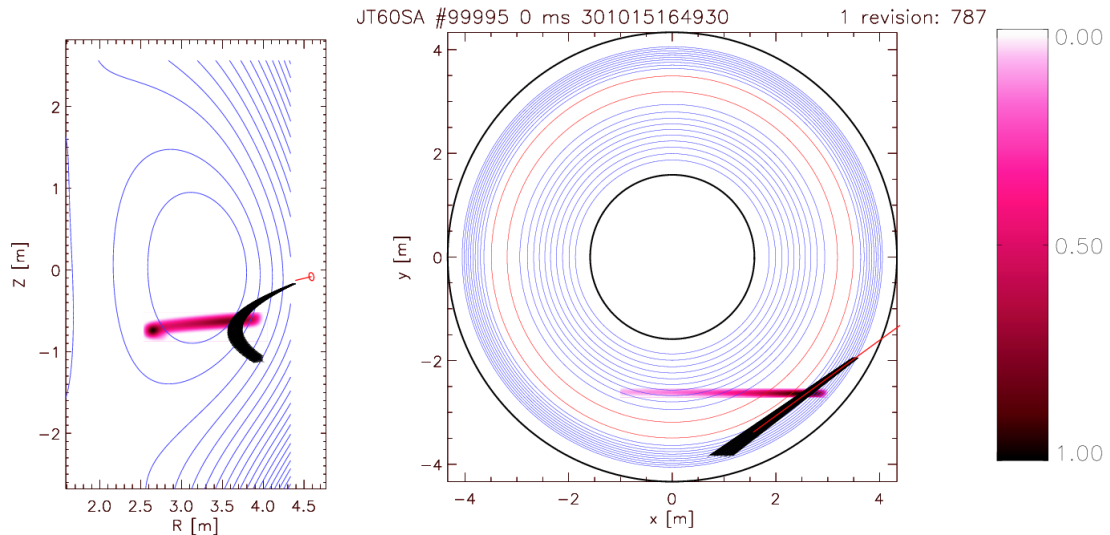


Figure 4.9: *Left image shows the poloidal cross-section. The right image shows the toroidal cross-section. The LOS for each detector are marked with black, the observation system and viewing direction marked with red.*

Figure 4.9 shows the location of the observation system on a poloidal cross-section as well on toroidal cross-section. The ideal location for the observation system for core observations on the upper N-NBI beam is located on port P-2, relatively close to the equatorial cross-section. A 23 cm portion of the beam is observed, where the emitted light intensity is the highest, between $30 - 53 \text{ cm}$ along the beam. The Doppler shift for the N-NBI beams is very high, of about $11 - 12 \text{ nm}$ red shifted for the current observation scenario, which puts the observed spectral line well beyond the C-II emission.

Figure 4.10 shows the detected light profile for the current observation scenario. The detected photon current increases slowly deeper into the plasma, suggesting the observed region to be just ahead of the maximal emission

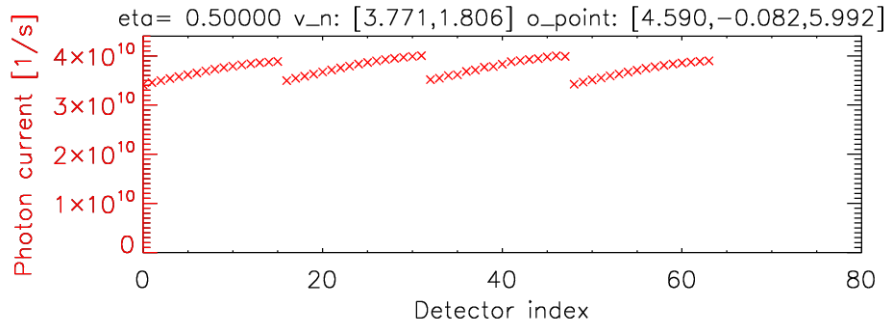


Figure 4.10: Shows the detected photon current for each detector channel.

area. The detected values nevertheless are higher than originally anticipated, 4×10^{10} 1/s, making the N-NBI beam a more favourable candidate for plasma core observations with regard to the co- or counter-tangential beam scenarios.

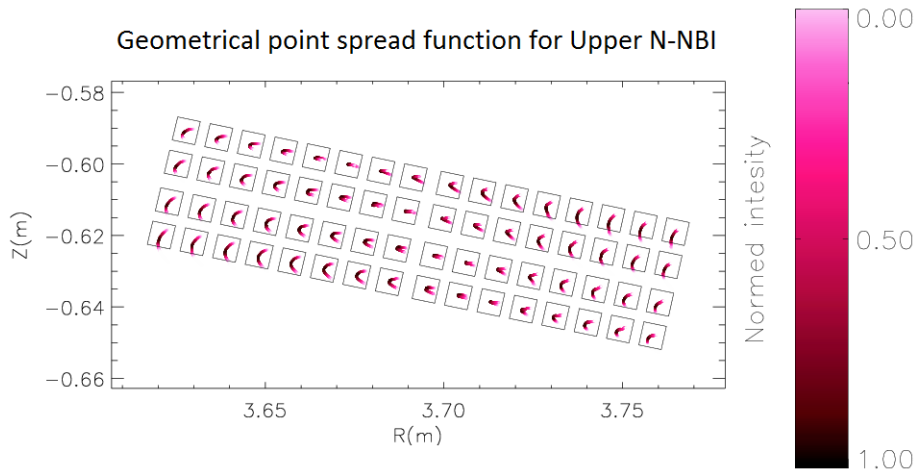


Figure 4.11: Shows the geometrical point spread function on a chosen poloidal plane. Purple marks the projected light emission for the LOS.

Figure 4.11 shows the geometrical point spread function for the current observation system. The radial and poloidal resolutions are determined by the measure of a smear for each LOS. The detector projections are marked as the black edged squares on the poloidal plane. The closer the LOS are to being parallel with the magnetic field lines the smaller the measure of the smear, indicating a very favourable spatial resolution for the current observation scenario.

Figure 4.12 confirms the spatial resolution, the average radial resolution is about 1.44 mm, while the averaged poloidal resolution is about 1.97 mm. The significantly smaller beam size (Table ??) has a strong contribution in

Spatial resolution calculation for the DBES diagnostics on JT-60SA

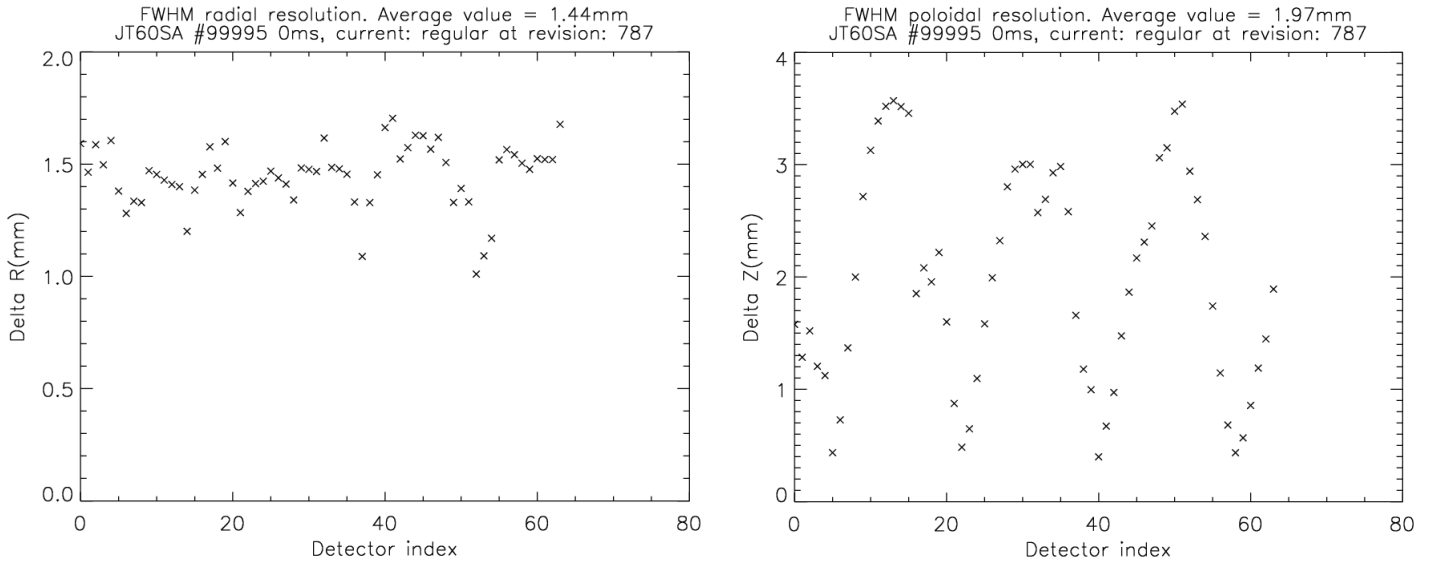


Figure 4.12: *Left image shows the radial resolution for each detector pixel for observation behind the beam. Right image shows poloidal resolution for observation behind the beam.*

the reduction of the spatial resolution with regard to the previously presented scenarios. Comparing the spatial resolution with the previous two scenarios, the N-NBI observation system is superior, however the emission smear is considerably higher. Simulations performed on the current scenario indicate a $10 - 7$ mm overall addition to the spatial resolution, which decreases as the beam penetrates deeper into the plasma.

Chapter 5

Conclusions and outlook

The RENATE simulation tool, which models beam emission spectroscopy (BES) diagnostics, has been used to determine the ideal positions for such observation system on the JT-60SA tokamaks' neutral beam injection (NBI) heating systems. In order to accomplish the task, I developed a new module to the simulation code. The newly developed **Optimal Observation** module has proven to be a useful asset for determining locations for ideal observation systems which are placed such as to have the least possible impact on the spatial resolution of the observation system by reducing the geometrical contribution to the spatial resolution. The module provides the necessary data to calculate locations of the observation points in question, as well as to study the effect of the observation point distribution for a certain beam and observation type. The added calculation of the Doppler shift for each possible observation point contributes to the selection of optimal observation locations.

Simulation were performed on the JT-60SA tokamaks' co- and counter-tangential NBI heating beams as well as on the negative ion source (N-NBI) beams, in order to determine the locations for optimal observation systems. During the study I have found that observation points located behind the beam tend to provide an overall better radial resolution compared to observation points in front of the beam. Simulations also suggest a slight trade-off in the overall poloidal and radial resolution if the beam is observed from the blue or red shifted side. Simulations of the observed Doppler shift have indicated that for all observation scenarios, the shift towards the larger wavelength is sufficient to avoid the C-II line, however beams #7 and #10 are preferred as well as the N-NBI beams, due to an increased shift. I gave three possible observation scenarios as a conclusion to the optimal observation simulations, upon which I performed a detailed spatial resolution study. The predictions made by the optimal observation module have been proven to

be accurate. For plasma edge observation, performed on counter-tangential beam #7A, the most suitable port would be P-17 providing, a sufficient amount of observed light compared to the observation located on port P-14, which has a slightly more degraded spatial resolution. The plasma center observation system, simulated on co-tangential beam #9B, is proposed to be placed on port P-3 providing adequate spatial resolution and detected light. The observation systems on P-3 and P-14 confirm the trade-off in radial and poloidal resolution, which is apparent only if the observation points for a certain region of the beam are sufficiently scattered. The observation system on port P-2 has provided the best spatial resolution so far on the upper N-NBI beam with a reasonable amount of detected light, making it a prime candidate for plasma core observations.

The optimal observation module has been developed out of necessity to ascertain locations for ideal observation systems in order to negotiate for port slots. At the completion of this study, no information has been made available with regard to the layout of the port plugs for the ports in question, nor regarding the availability of these ports. The data presented in the current study serves as a first order approximation for the potential locations for observation systems. The next step is to choose observation points with regard to the port layouts that should be made available and perform detailed studies regarding light detection, spatial resolution as well as fluctuation measurements for the locations in question. Due to the high number of NBI systems (16 perpendicular, 8 tangential and 2 N-NBI beams) on the JT-60SA tokamak, it is important to provide observation points with LOS that intersect and potentially collect light from as few additional neutral beams as possible, in order to reduce interference with other beams.

Acknowledgements

I would like to thank my supervisor, dr. Pokol Gergő, for his support during my work. This work has been carried out within the framework of the EU-ROfusion Consortium and has received funding from the European Union's Horizon 2020 research and innovation programme under grant agreement number 633053. The views and opinions expressed herein do not necessarily reflect those of the European Commission. I also acknowledge the support of the Hungarian State grant NTP-TDK-14-0022.

Bibliography

- [1] I.Pusztai, G.I.Pokol, D.I.Réfy, S.Zoletnik, D.Dunai, G.Anda, J.Schweitzer, "Deconvolution-based correction of alkali beam emission spectroscopy density profile measurement", *Review of Scientific Instruments*, Vol. **80**: 083 - 502, 2009.
- [2] D.Guszejnov, G.I.Pokol, I.Pusztai, D.I.Réfy, S.Zoletnik, M.Lampert, Y.U.Nam, "Three dimensional modeling of beam emission spectroscopy measurements in fusion plasmas", *Review of Scientific Instruments*, Vol. **83**: 113 -501, 2012.
- [3] Ö.Asztalos, "Spatial resolution calculation for the BES system on the EAST tokamak", *BME, Diploma Thesis*, 2015.
- [4] J.P.Freiberg, "Plasma Physics and Fusion Energy", *Cambridge University Press*, 2007.
- [5] J.A.Bittencourt, "Fundamentals of Plasma Physics", *Springer Science and Business Media*, 325-352, 2004.
- [6] R. Klieber, R. Bilato, "IPP Summer University for Plasma Physics", *Greifswald*, 2011.
- [7] T.A.Heltemes, G.A.Moses, J.F.Santarius, "Analysis of an Improved Fusion Reaction Rate Model for Use in Fusion Plasma Simulations", *Fusion Technology Institute*, University of Wisconsin, 2005.
- [8] I.Pusztai, "Fúziós berendezések atomnyaláb diagnosztikájának modellezése", *BME, MSc Diplomamunka*, 2007.
- [9] G.I.Pokol, "Introduction into fusion plasma physics", *BME Course*, 2012.
- [10] M.Mahdavi, E.Asadi, "Estimates of Tritium Produced Ratio in the Blanket of Fusion Reactors", *Open Journal of Microphysics*, Vol. **3**: 8-11, 2013.

- [11] S.Atzeni, J.Meyer ter Vehn, "The Physics of Inertial Fusion", *Calerdon Press Oxford*, 2004.
- [12] J.Wesson, "Tokamaks", *Calerdon Press Oxford*, 2004.
- [13] J.Wesson, "Science of JET", *JET, Joint Undertaking, Abingdon, Oxon*, 2000.
- [14] F.F.Chen, "Introduction to Plasma Physics and Controlled Fusion", *Plenum Press, New York*, 1984.
- [15] E.Pietroa, P.Barabaschia, Y.Kamadab, S.Ishidac, JT-60SA Team, "Overview of engineering design, manufacturing and assembly of JT-60SA machine", *Fusion Engineering and Design*, Vol. **89**: 2128-2135, 2014.
- [16] J.Bucalossi, "JT-60SA ITER Satellite Tokamak Program of JA-EU", *3rd Karlsruhe International School on Fusion Technologies*, 2009.
- [17] B.Schweer, "Application of atomic beams for plasma diagnostics", *Fusion Science and Technology*, Vol. **49**: 404-411, 2006.
- [18] B.Schweer, "Application of Atomic Beams in Combination with Spectroscopic Observation for Plasma Diagnostic", *Fusion Science and Technology*, Vol. **53**: 425-432, 2008.
- [19] M.Kikuchi, K.Lackner, M.Q.Tran, "Fusion physics", *IAEA:571-600, Vienna*, 2012.
- [20] Ö.Asztalos, K.Z.Németh, G.I.Pokol, "Feasibility study of Alkali BES system on W7-X", *BME, Report*, 2015.
- [21] E.Wolfrum, J.Schweinzer, D.Bridi, K.Igenbergs, J.Kamleitner, F.Aumayr, ASDEX Upgrade team, "A sodium (Na) based edge diagnostic" *Journal of Nuclear Materials*, Vol. **390-391**: 1110 - 1113, 2009.
- [22] R.Gutser, D.Wünderlich, U.Fantz, NNBI-Team, "Negative Hydrogen Ion Transport in RF-driven Ion Sources for ITER NBI", *Plasma Phys. Control. Fusion*, Vol. **53**: 105014, 2011.
- [23] D.Guszejnov, "Atomnyaláb-emissziós plazma diagnosztika fejlesztésének támogatása szimulációk segítségével", *BME, Bsc Diploma thesis*, 2011.

- [24] D. Guszejnov, G. I. Pokol, I. Pusztai, D. Réfy, "Applications of the RENATE beam emission spectroscopy simulator", *38th EPS, Conference on Plasma Physics*, 2011.
- [25] D.I.Réfy, "Opitkai modul fejlesztése a RENATE atomnyaláb szimuláció programcsomaghoz", *BME, Msc Diploma thesis*, 2011.
- [26] Ö. Asztalos, G.I.Pokol, "BES modeling with the RENATE simulation tool", *7th HPPW Conference, Tengelic*, 2015.
- [27] D. I.Réfy, G. I. Pokol, D. Dunai, S. Zoletnik, M. Lampert, Ö. Asztalos, D. Guszejnov, "Spatial resolution modelling of various beam emission spectroscopy experiments", *41st EPS, Conference on Plasma Physics*, 2014.
- [28] Ö.Asztalos, "Atomnyaláb emissziós diagnosztikák térbeli felbontásának meghatározása a RENATE szimulációs kód alkalmazásával", *TDK, BME*, 2014.
- [29] Y.C.Ghim, A.R.Field, S.Zoletnik, D.Dunai, "Calculation of spatial resolution of 2D beam emission spectroscopy diagnostic on MAST", *Review of Scientific Instruments*, Vol. **81**: 10D - 713, 2010.
- [30] A.R.Field, D.Dunai, R.Gaffa, Y.C.Ghim, I.Kiss, "Beam emission spectroscopy turbulence imaging system for the MAST spherical tokamak", *Review of Scientific Instruments*, Vol. **83**: 013 - 508, 2012.
- [31] JT-60SA Research Unit, "JT-60SA Research Plan", *version 3.0*, 2011.
- [32] Y.Kamada, P.Barabaschi, S.Ishida, JT-60SA Team, "Progress of the JT-60SA Project" *Nucl. Fusion*, Vol. **53**, 104010, 2013.
- [33] M.Hanada, N.Akino, Y.Endo, T.Inoue, M.Kawai, M.Kazawa, K.Kikuchi, M.Komata, A.Kojima, K.Mogaki, S.Nemoto, K.Noto, K.Oasa, K.Oshima, S.Sasaki, T.Simizu, Y.Tanaka, N.Umeda, K.Usui, K.Watanabe and L.R.Grisham, "Development and design of the negative-ion-based NBI for JT-60 Super Advanced", *J.Plasma Fusion Res.*, Vol. **9**: 208-213, 2010
- [34] D.Guszejnov, G.I.Pokol, "Feasibility Study of the Fluctuation Beam Emission Spectroscopy in KSTAR", *BME Report*, 2011.
- [35] T. Soetensa, R. Jaspersa, E. Desopperea, "The motional Stark effect diagnostic on TEXTOR-94: First measurements", *Review of Scientific Instruments*, Vol. **70**: 001 - , 1999.